Title
Highly Tunable Magnetic Phases in Transition-Metal Dichalcogenide Fe1/3+δNbS2

Journal
Physical Review X, 12(2)

ISSN
2160-3308

Authors
Wu, Shan
Xu, Zhijun
Haley, Shannon C
et al.

Publication Date
2022-04-01

DOI
10.1103/physrevx.12.021003

Peer reviewed

Important Notice to Authors

No further publication processing will occur until we receive your response to this proof.

Attached is a PDF proof of your forthcoming article in *Physical Review X*. The article accession code is XF10524.

Your paper has been assigned the following Subject Area labels: Condensed Matter Physics, Magnetism

Your paper will be in the following section of the journal: RESEARCH ARTICLES

Please note that as part of the production process, APS converts all articles, regardless of their original source, into standardized XML that in turn is used to create the PDF and online versions of the article as well as to populate third-party systems such as Portico, Crossref, and Web of Science. We share our authors' high expectations for the fidelity of the conversion into XML and for the accuracy and appearance of the final, formatted PDF. This process works exceptionally well for the vast majority of articles; however, please check carefully all key elements of your PDF proof, particularly any equations or tables.

Figures submitted electronically as separate files containing color appear in color in the journal.

Specific Questions and Comments to Address for This Paper

The numbered items below correspond to numbers in the margin of the proof pages pinpointing the source of the question and/or comment. The numbers will be removed from the margins prior to publication.

1. Second proof: Please carefully confirm that all first-proof corrections were addressed and that changes were made accurately.
2. Second proof: Please note that in accordance with PRX Journal Style Guidelines acronyms are defined at the first occurrence in abstract or body section only if the acronym appear three or more than three times.
3. Second proof: Please provide title for APPENDIX (APPENDIX:____) like other section headings “INTRODUCTION,” “EXPERIMENTAL PROCEDURES,”....., “CONCLUSIONS”..etc.
4. Second proof: Please note that Ref. [57] is updated in accordance with PRX Journal Style Guidelines. Hence, the requested correction could not be made.
5. Second proof: Please check and approve that the paper is ready to be published in its current form.

ORCIDs

Please follow any ORCID links (ID) after the authors’ names and verify that they point to the appropriate record for each author.

Crossref Funder Registry ID:

Information about an article's funding sources is now submitted to Crossref to help you comply with current or future funding agency mandates. Crossref's Funder Registry (https://www.crossref.org/services/funder-registry/) is the definitive registry of funding agencies. Please ensure that your acknowledgments include all sources of funding for your article following any requirements of your funding sources. Where possible, please include grant and award ids. Please carefully check the following funder information we have already extracted from your article and ensure its accuracy and completeness:

- U.S. Department of Energy, FundRef ID http://dx.doi.org/10.13039/100000015 (US/United States)
- Office of Science, FundRef ID http://dx.doi.org/10.13039/100006132 (US/United States)
- Basic Energy Sciences, FundRef ID http://dx.doi.org/10.13039/100006151 (US/United States)

- Oak Ridge National Laboratory, FundRef ID http://dx.doi.org/10.13039/100006228 (US/United States)

Other Items to Check

- Please note that the original manuscript has been converted to XML prior to the creation of the PDF proof, as described above. Please carefully check all key elements of the paper, particularly the equations and tabular data.
- Please ignore the text of the Popular Summary, it is not the final version. An APS science writer will work with you separately to edit the summary.
- Title: Please check; be mindful that the title may have been changed during the peer-review process.
- Author list: Please make sure all authors are presented, in the appropriate order, and that all names are spelled correctly.
- Please make sure you have inserted a byline footnote containing the email address for the corresponding author, if desired. Please note that this is not inserted automatically by this journal.
- Affiliations: Please check to be sure the institution names are spelled correctly and attributed to the appropriate author(s).
- Receipt date: Please confirm accuracy.
- Acknowledgments: Please be sure to appropriately acknowledge all funding sources.
- Hyphenation: Please note hyphens may have been inserted in word pairs that function as adjectives when they occur before a noun, as in "x-ray diffraction," "4-mm-long gas cell," and "*R*-matrix theory." However, hyphens are deleted from word pairs when they are not used as adjectives before nouns, as in "emission by x rays," "was 4 mm in length," and "the *R* matrix is tested."
  Note also that Physical Review follows U.S. English guidelines in that hyphens are not used after prefixes or before suffixes: superresolution, quasiequilibrium, nanoprecipitates, resonancelike, clockwise.
- Please check that your figures are accurate and sized properly. Make sure all labeling is sufficiently legible. Figure quality in this proof is representative of the quality to be used in the online journal. To achieve manageable file size for online delivery, some compression and downsampling of figures may have occurred. Fine details may have become somewhat fuzzy, especially in color figures. Figures to be published in color online will appear in color on these proofs if viewed on a color monitor or printed on a color printer.
- Overall, please proofread the entire *formatted* article very carefully. The redlined PDF should be used as a guide to see changes that were made during copyediting. However, note that some changes to math and/or layout may not be indicated.

Ways to Respond

- ***Web:*** If you accessed this proof online, follow the instructions on the web page to submit corrections.
- ***Email:*** Send corrections to aps-robot@luminad.com. Include the accession code XF10524 in the subject line.
- ***Fax:*** Return this proof with corrections to +1.855.808.3897.

If You Need to Call Us

You may leave a voicemail message at +1.855.808.3897. Please reference the accession code and the first author of your article in your voicemail message. We will respond to you via email.

Popular Summary

Antiferromagnets are a special class of magnetic materials in which the atomic magnetic moments alternate in direction, resulting in a macroscopically zero net moment. Their consequent insensitivity to external magnetic fields makes these materials promising for building spintronic devices, which store and transfer information in electron spins rather than just charge. One such material, the "van der Waals" antiferromagnet $Fe_{1/3+\delta}NbS_2$, has shown intriguing spintronic behavior: a

rapid current-induced resistance switching that couples to the antiferromagnetism. But the magnetic properties underlying the resistance were unknown. Here, we report on highly tunable magnetic states in this material that are controlled by magnetic defects. Such defects typically inhibit magnetism because of the disorder, rather than creating new functionality.

We perform comprehensive neutron diffraction measurements on crystals with varying abundances of iron. We find that the microscopic magnetic moments arrange themselves into two dramatically distinct configurations at individual atomic sites between the extremes of the iron abundances. These results demonstrate that there are nearly degenerate energies for the two magnetic states involved in the switching. These experimental results are strongly supported by our theoretical calculations. We are thus able to determine that the rapid change of the states as a function of iron ratio underlies the tunable resistance switching, thereby providing crucial insights that form the basis for understanding the spintronic behavior.

Our work will stimulate more exploration on such unusual antiferromagnetic spintronic behavior and provide a new avenue for defect-induced controllability of the magnetic state in other van der Waals systems. That should, in turn, enable device scientists to design the very best materials for the spintronic devices of the future.

Highly Tunable Magnetic Phases in Transition-Metal Dichalcogenide $Fe_{1/3+\delta}NbS_2$

Shan Wu,[1,2,*] Zhijun Xu,[3,4] Shannon C. Haley,[1,2] Sophie F. Weber,[1,2,‡] Arani Acharya,[1] Eran Maniv,[1,2,5] Yiming Qiu,[3] A. A. Aczel,[6] Nicholas S. Settineri,[7] Jeffrey B. Neaton,[1,8,2] James G. Analytis,[1,2] and Robert J. Birgeneau[1,2,†]

[1]*Department of Physics, University of California, Berkeley, California 94720, USA*
[2]*Material Sciences Division, Lawrence Berkeley National Lab, Berkeley, California 94720, USA*
[3]*NIST Center for Neutron Research, National Institute of Standards and Technology, Gaithersburg, Maryland 20899, USA*
[4]*Department of Materials Science and Engineering, University of Maryland, College Park, Maryland 20742, USA*
[5]*Department of Physics, Ben-Gurion University of the Negev, Beer-Sheva 84105, Israel*
[6]*Neutron Scattering Division, Oak Ridge National Laboratory, Oak Ridge, Tennessee 37831, USA*
[7]*Department of Chemistry, University of California, Berkeley, California 94720, USA*
[8]*Kavli Energy Nanosciences Institute at Berkeley, Berkeley, California 94720, USA*

(Received 2 June 2021; revised 2 February 2022; accepted 3 February 2022)

Layered transition-metal dichalcogenides (TMDCs) host a plethora of interesting physical phenomena ranging from charge order to superconductivity. By introducing magnetic ions into $2H$-TA_2 (T = Nb, Ta; A = S, Se), the material forms a family of magnetic intercalated TMDCs M_xTA_2 ($M = 3d$ transition metal). Recently, $Fe_{1/3+\delta}NbS_2$ has been found to possess intriguing resistance switching and magnetic memory effects coupled to the Néel temperature of $T_N \sim 45$ K [Maniv *et al.*, Nat. Phys. **17**, 525 (2021); Sci. Adv. **7**, eabd8452 (2021)]. We present comprehensive single crystal neutron diffraction measurements on underintercalated ($\delta \sim -0.01$), stoichiometric, and overintercalated ($\delta \sim 0.01$) samples. Magnetic defects are usually considered to suppress magnetic correlations and, concomitantly, transition temperatures. Instead, we observe highly tunable magnetic long-ranged states as the Fe concentration is varied from underintercalated to overintercalated, that is, from Fe vacancies to Fe interstitials. The under- and overintercalated samples reveal distinct antiferromagnetic stripe and zigzag orders, associated with wave vectors $k_1 = (0.5, 0, 0)$ and $k_2 = (0.25, 0.5, 0)$, respectively. The stoichiometric sample shows two successive magnetic phase transitions for these two wave vectors with an unusual rise-and-fall feature in the intensities connected to k_1. We ascribe this sensitive tunability to the competing next-nearest neighbor exchange interactions and the oscillatory nature of the Ruderman-Kittel-Kasuya-Yosida mechanism. We discuss experimental observations that relate to the observed intriguing switching resistance behaviors. Our discovery of a magnetic defect tuning of the magnetic structure in bulk crystals $Fe_{1/3+\delta}NbS_2$ provides a possible new avenue to implement controllable antiferromagnetic spintronic devices.

DOI: Subject Areas: Condensed Matter Physics, Magnetism

I. INTRODUCTION

Layered magnetic van der Waals (vdW) materials have recently attracted tremendous interest, resulting in rapid progress in fundamental studies of novel vdW physical phenomena together with promising potential for spintronic applications [1–4]. The weak van der Waals bonds make single crystals readily cleavable thereby offering a new platform to study the evolution of the behavior from three dimensions (3D) down to the 2D limit. Moreover, the wide flexibility of 2D atomic samples allows for an efficient manipulation of magnetic states through external perturbations, such as strain, gating, proximity effect, and pressure [5–8]. In bulk magnetic vdW crystals, usually high hydrostatic pressure [9,10] or significant chemical substitution [11,12] is utilized to modulate the magnetic state or the effective dimensionality via tuning of the interlayer exchange couplings. Magnetic defects are typically

*shanwu@berkeley.edu
†robertjb@berkeley.edu
‡Present address: Department of Materials, ETH Zurich, CH-8093 Zürich, Switzerland.

considered to be responsible for inhibiting long-range magnetism due to the atomic-scale disorder. Here we demonstrate novel behavior in which magnetic defects tune the magnetic ground states in the transition-metal dichalcogenide (TMDC) bulk crystal $Fe_{1/3+\delta}NbS_2$.

$Fe_{1/3+\delta}NbS_2$ is a member of a large class of intercalated TMDCs, M_xTA_2 family ($M = 3d$ transition metal; $T =$ Nb, Ta; $A =$ S, Se) [13,14]. The host material is a prototypical example of a charge density wave system; recently, these systems have been attracting major attention because of other exotic properties, such as possible quantum spin liquid phases and 2D superconductivity [15–20]. The vdW bonding between chalcogen atoms of adjacent $2H$-TA_2 layers allows the ready intercalation of magnetic atoms. The intercalated atoms order into a stacked $\sqrt{3} \times \sqrt{3}$ superlattice when $x = 1/3$ [21]. This family of compounds shares the same crystal structure with a noncentrosymmetric space group $P6_322$ and a bilayer triangular arrangement of the intercalated atoms [Figs. 1(a) and 1(b)]. The broken inversion symmetry results in a Dzyaloshinskii-Moriya (DM) interaction between planes allowing an in-plane moment in addition to the competing bilinear exchange interactions with their concomitant geometric frustration. In addition, as a metallic system, there is a strong interaction between the conduction electrons and the local moments via the Ruderman-Kittel-Kasuya-Yosida (RKKY) mechanism. Depending on the host $2H$-TA_2 layer and the intercalated species, the family exhibits a fascinating variety of magnetic and electronic properties [22–30] in bulk samples.

In the intercalated variant $M_{1/3}NbS_2$ subgroup, chiral helimagnetism was observed for the Cr and Mn species [24–28,31]; the V version exhibits a spin structure characterized by ferromagnetic planes stacked antiferromagnetically with canted in-plane moments [30,32]; the Co version shows a stripe order with spins directing in the *ab* plane [29]. Novel physical properties were reported in these species, including the anomalous Hall effect, an electrical magnetochiral effect, and magnetic soliton confinement [33–35]. Most materials in this family are characterized by an easy-plane anisotropy and mostly dominant ferromagnetic interactions. In contrast, the intercalated Fe version displays predominantly antiferromagnetic (AFM) correlations and a strong easy-axis anisotropy [13,36,37].

Recently, a resurgence of interest in the Fe version has been sparked by the demonstration of intriguing spintronic properties in bulk $Fe_{1/3+\delta}NbS_2$ crystals [38,39]. Both current-induced resistance switching and magnetic memory effects were reported below the Néel transition temperature $T_N \sim 45$ K. Moreover, the relevant spintronic properties were found to depend sensitively on the intercalation ratio x ($=1/3 + \delta$) [40]. By decreasing the ratio slightly below $1/3$, the system exhibited a much more prominent spintronic response concomitant with dramatic spin-glass-like behavior below the AFM Néel temperature. There are so far only a few known examples of current-induced switching behavior in AFM single crystal compounds [41,42]. The mechanism is believed to entail an applied current inducing a spin polarization due to the combination of the breaking of inversion symmetry and Rashba spin-orbit coupling [43]. It has been argued that the reported resistance switching in the off-stoichiometric sample of $Fe_{1/3+\delta}NbS_2$ somehow relates to the observed spin-glass behavior [38,40], thence providing a possible new way to explore AFM spintronic devices. Therefore, a complete understanding of the magnetic ground states and magnetic correlations as a function of the intercalation ratio is essential to uncover the mechanism of the observed interesting spintronic properties. Further, the only relevant information about the magnetic structures which currently exists derives from neutron powder diffraction measurements carried out decades ago at low temperatures [44]. In addition to the spintronic motivation, this system is of intrinsic interest as a vdW material with interesting and, as we shall see, novel magnetic properties.

In this paper, we report detailed neutron scattering measurements on high-quality single crystals of Fe-intercalated TMDC $Fe_{1/3+\delta}NbS_2$ with x spanning $1/3$. Surprisingly, we found highly tunable magnetic phases in the bulk crystal that are more versatile than the single phase reported in previous work. By a comprehensive experimental investigation together with modeling of the magnetic structures, we determined two long-ranged antiferromagnetically ordered states and that one can tune from one state to the other by varying x subtly from less than to greater than $1/3$, that is, by varying from Fe vacancies to Fe interstitials ($\delta \sim \pm 0.01$). The stoichiometric sample with

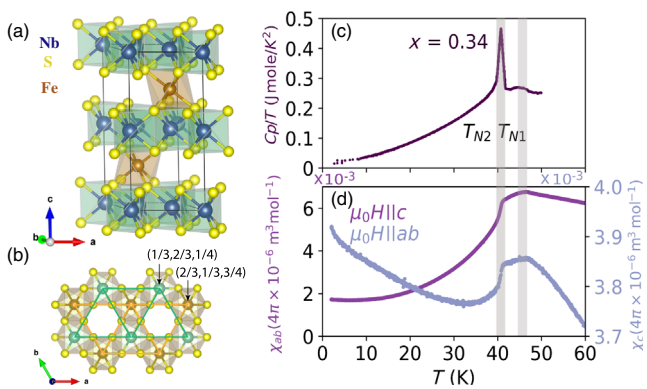

FIG. 1. (a) Crystallographic structure of $Fe_{1/3}NbS_2$. Fe atoms occupy $2c$ Wyckoff positions, forming a bilayer triangular lattice with a noncentrosymmetric space group $P6_322$. (b) The view in the *ab* plane showing only Fe and S atoms. Orange and green spheres represent two Fe triangular lattice layers with different *c*-axis coordinates marked in the figure. (c) Representative specific heat and (d) magnetization measurement with applied field $\mu_0 H = 0.1$ T (T) in the low temperature region for $x = 0.34$ sample. The shaded regions mark two anomalies, identified as antiferromagnetic transitions by neutron scattering measurements. For other samples, see the Appendix.

$x = 1/3$, on the other hand, exhibits both magnetic structures characterized by two successive magnetic phase transitions upon cooling. In Sec. IV, we discuss this tunability and its implications to the fascinating spintronic behavior exhibited by these materials. This finding is the first example of such unusual switching and exchange bias behaviors in the intercalated TMDCs M_xTA_2 family; it can provide an archetypal case for magnetic defect-induced switching of the magnetic state in bulk magnetic vdW systems.

II. METHODS

High-quality single crystals were synthesized using a chemical vapor transport method with a polycrystalline precursor made from Fe, Nb, and S elements in the ratio of $x:1:2$ [21]. The crystals used in this paper are not the same ones made into devices in Ref. [40], but sizable pieces either from the same batch or grown for the neutron diffraction experiments by the same recipes and experimental setups. We weighed the initial Fe powders with calculating the ratio of $x = 0.29, 0.3, 0.32, 0.34$. The values of the resulting intercalation ratio x of individual single crystals were determined by energy dispersive x-ray spectroscopy (EDX) (Fig. 14). By measuring ~20 points for each crystal, the mean value for each crystal is $x = 0.31$, 0.32, 0.33, 0.35. The slightly larger values of the mean ratio is due to systematic shifts. The standard deviation for each crystal is 0.003, 0.003, 0.005, 0.003, respectively. But considering other errors from the instrument, the estimated error is ± 0.01 for our crystals used in neutron scattering. The ratio of $x = 0.34$ crystal was formally determined by Maniv *et al.* [38,40]. The actual values of x were confirmed with higher accuracy (to the third decimal place) from inductively coupled plasma optical emission spectroscopy measurements [38]. Though the change of ratio is subtle, the system shows a rapid change in the bulk characterizations and spintronic properties [40]. As we see later in the paper, the neutron scattering measurements represent a surprising tunability of spin structures on the individual samples, on the other hand confirming the accuracy of the relative values of the ratios up to ± 0.01.

Room temperature single crystal x-ray diffraction (XRD) patterns were measured at the ChemXray facility, UC Berkeley. Magnetization measurements were performed using a Quantum Design MPMS-3 system. The heat capacity was measured in a Quantum Design PPMS system [45]. Neutron scattering experiments were carried out at several instrumental stations. Single crystal diffraction mapping at temperatures $T = 38$ and 5 K with coaligned crystals (mosaicity ~5°) in the range of $x = 0.32$–0.34 employed the MACS spectrometer at NCNR [46]. The data were collected with $E_f = 5$ meV with a double focusing monochromator and a Be filter placed before and after the sample. To investigate accurately the tunable magnetic state, single crystal neutron diffraction measurements with one crystal were carried out on SPINS, BT-7 at NCNR, and HB1A at HFIR for different intercalation ratios: $x = 0.31$, 0.32, 0.33, 0.34, and 0.35 with masses of 12, 23, 9, 3, and 27 mg, respectively. Measurements were conducted with a PG (002) monochromator and analyzer using $E_f = 5$, 14.7, and 14.48 meV neutrons on SPINS, BT-7, and HB1A, respectively. We discuss the density functional theory (DFT) calculation strongly related to our experimental results. The DFT calculations utilized the Perdew-Burke-Ernzerhof (PBE) functional and added a Hubbard U correction accounting for the Fe d electrons. For details of the DFT calculations, see Ref. [47].

III. EXPERIMENTAL RESULTS

A. Crystal structures and magnetization

The crystallographic structure of $Fe_{1/3}NbS_2$ is identical to that of other species in this family, described by the space group $P6_322$, with a triangular sublattice of iron ions intercalated in the honeycomb 2H-NbS_2 [Fig. 1(a)]. One crystallographic unit cell contains two equivalent iron sites at coordinates $(1/3, 2/3, 1/4)$ and $(2/3, 1/3, 3/4)$, respectively, associated with the $2c$ Wyckoff positions. They occupy the vacant octahedral sites stacking between the prismatic NbS_2 layers and form two triangular superlattice planes [Fig. 1(b)]. The shifted stacking between the two layers leads to a noncentrosymmetric structure. The single crystal x-ray diffraction pattern has been refined in the space group $P6_322$ with R_1 value of 3.44%, with the atomic coordinates listed in Table IV. This is consistent with a previous report [21]. As for other intercalated species, the intercalated ions are allowed to occupy $2b$ and $2d$ sites, leading to occupational disorder [48]. However, in our Fe materials this issue is not a severe problem. The major Fe occupancy occurs at the $2c$ sites with a minor ratio at the $2b$ sites (Table IV in the Appendix). The x-ray diffraction pattern manifests sharp three-dimensional peaks in both the $(H0L)$ and $(HK0)$ planes (Fig. 13) and also from neutron experiments for all the samples, suggesting a minimum Fe lattice disorder.

In the slightly off-stoichiometric samples, the noncentrosymmetric structure with the space group $P6_322$ is unchanged from our single crystal XRD analysis. The underintercalated sample $x = 0.32$ reveals the vacancies at the $2c$ Wyckoff positions with a little occupancy at the $2b$ sites. The overintercalated sample ($x = 0.35$) allows a larger number of occupancy at the $2b$ sites for additional Fe intercalations. Both ratios, where we detected magnetic ordering, preserves a majority of well-ordered Fe lattice, also demonstrated by the sharp 3D Bragg peaks from neutron scattering and the transmission electron spectroscopy measurements [38]. The $x = 0.31$ sample shows some disorder with the occupancy value of 0.1 at the $2b$ sites (Table IV). The detailed information of structure analysis for all the ratios are presented in the Appendix. In all, our crystals

reveal a homogeneous distribution of Fe atoms (EDX measurements in the Appendix) and well-ordered lattice with respect to the sharp 3D peaks with the structure unaffected by varying the Fe ratio. We also point out that, as shown later, the sharp change occurring at particular the critical ratio of $1/3$ suggests a minimal occupational disorder. At the same time, surprisingly they show rapid changes in the magnetization and spin structures determined by neutron scattering measurements as described next.

The unintercalated host is a d-band metal with one electron on the Nb ion. Charge transfer from the Fe ions to the Nb band results in divalent oxidation states of the Fe with localized d electrons on the intercalated Fe ions [13]. We present magnetic susceptibility and specific heat measurements for the $x = 0.34$ sample in Figs. 1(c) and 1(d). Two successive anomalies occur at $T_{N1} \sim 45$ K and $T_{N2} \sim 41$ K; these features are also observed in the specific heat data. Curie-Weiss fits to the magnetic susceptibility in the paramagnetic region [Fig. 2(b)] yield values for the paramagnetic effective moment $\mu_{\rm eff} = 4.3(2)\mu_B$ and Curie-Weiss temperature $\theta_{\rm CW} = -49(1)$ K along the c axis; $\mu_{\rm eff} = 4.0(2)\mu_B$ and $\theta_{\rm CW} = -143(2)$ K in the ab plane. These values are consistent within the range of previous reports [22,23,36,44,49] with effective spin $S = 2$. The negative Curie-Weiss temperature suggests that antiferromagnetic exchange interactions are dominant. The derived single-ion anisotropy D is approximately 2 meV [50]. In the off-stoichiometric sample with $x < 1/3$, one transition was identified [40]; and a bifurcation between zero-field-cooled (ZFC) and field-cooled (FC) susceptibility data was observed, indicating spin-glass-like behavior. In the $x > 1/3$ sample, a small bifurcation between ZFC and FC data was observed below $T_f \sim 10$ K [40]. The characterizations of other single crystals used for neutron diffraction experiments in this paper are shown in the Appendix (Fig. 15). Highly anisotropic magnetization was observed in all magnetically ordered samples (Fig. 2). The sensitivity to the intercalation ratio x of the bulk magnetic and thermodynamic properties, as well as the associated intriguing spintronic properties, clearly calls for a detailed experimental study of the x dependence of the magnetic ground states in this bilayer triangular lattice system.

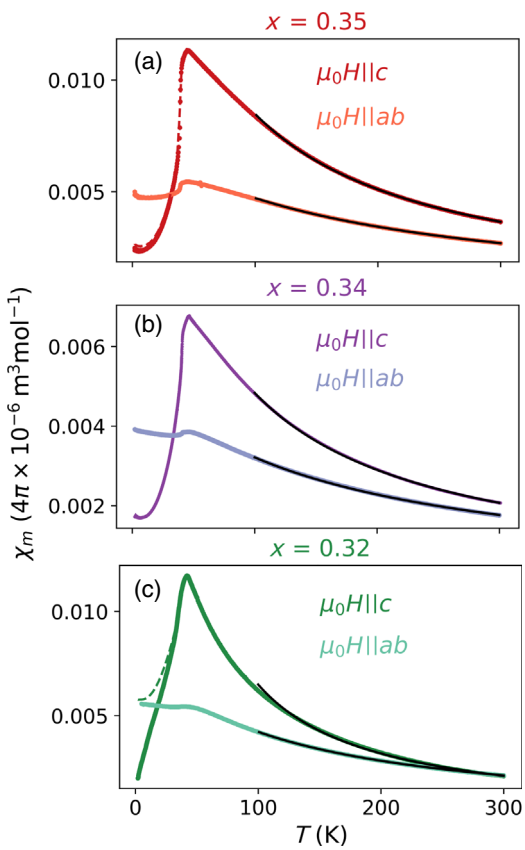

FIG. 2. Representative magnetization measurements in the full temperature region with an applied field $\mu_0 H = 0.1$ T along the c axis and in the ab plane for (a) $x > 1/3$, (b) x close to $1/3$, and (c) $x < 1/3$ sample. The dashed and solid lines correspond to the measurements with field-cooled and zero-field-cooled processes, respectively. The solid black lines are the results of the Curie-Weiss fits with the fitting range between 100 and 300 K.

B. Neutron scattering measurements

We first employed neutron diffraction scattering measurements in the $(HK0)$ scattering plane to study magnetic transitions for an assembly of coaligned crystals with x in the range of 0.32 to 0.34. These experiments were carried out at MACS, which is well suited for a broad momentum survey. The diffraction pattern, with the data at $T = 60$ K ($>T_N$) subtracted clearly shows two antiferromagnetic phases [Figs. 3(a) and 3(b)]. At $T = 38$ K, superlattice peaks are observed at wave vector transfer Q's associated with the propagation wave vector $\mathbf{k_1} = (0.5, 0, 0)$. At $T = 2$ K, another phase associated with the second propagation wave vector $\mathbf{k_2} = (0.5, 0.25, 0)$ appears leading to additional magnetic Bragg peaks. The pattern displays a sixfold symmetry; this is the result of three magnetic domains with Z_3 symmetry. From the measurements, the most intense peaks associated with $\mathbf{k_1}$ and $\mathbf{k_2}$ have wave vector transfers of $\mathbf{Q_1} = (0.5, 0.5, 0)$ (or 6 equivalent positions) and $\mathbf{Q_2} = (0.25, 0.5, 0)$ (or 12 equivalent positions), respectively.

The measurement on MACS were carried out on a set of coaligned single crystals. To obtain more information and specifically to elucidate the x dependence of the magnetic structures, we measured individual high-quality single crystals close to stoichiometry ($x = 0.33$, 0.34), underintercalated ($x = 0.31$, 0.32), and overintercalated ($x = 0.35$).

1. Nearly stoichiometric $x = 1/3$ sample

We measured two crystals with $x = 0.33$ and 0.34 separately at SPINS and BT7. Representative transverse and longitudinal, namely, θ and $\theta - 2\theta$, scans at 5 K are shown in Figs. 3(e) and 3(f). For the $x = 0.34$ sample, the

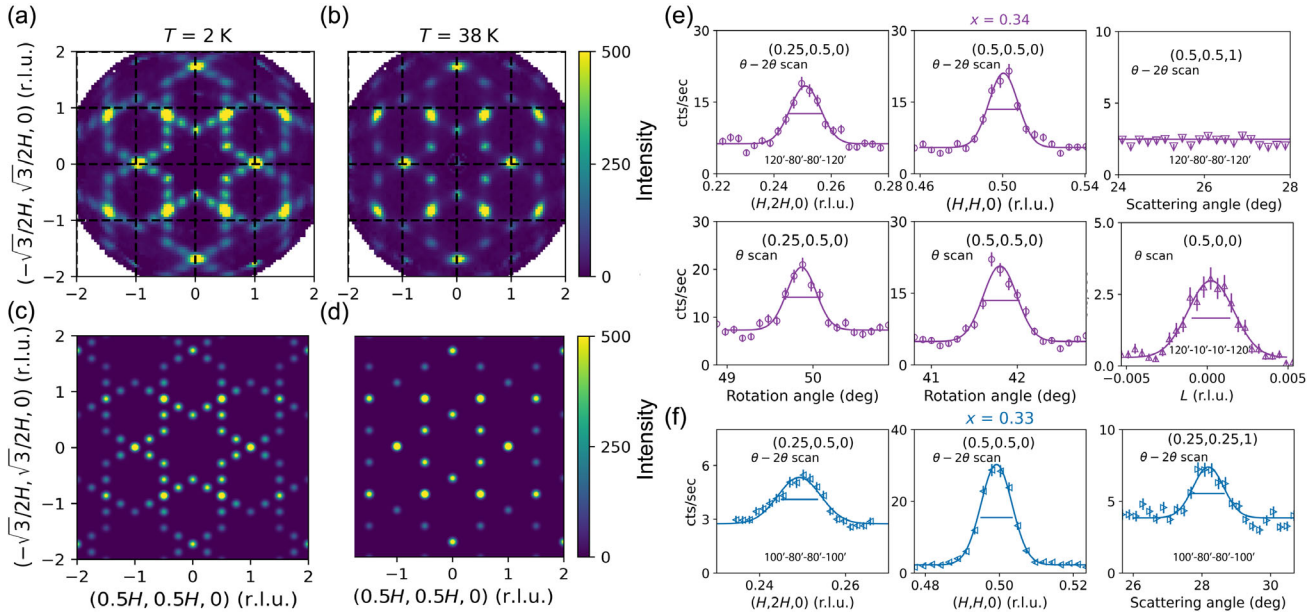

FIG. 3. (a),(b) Symmetrized single crystal neutron diffraction patterns collected at MACS by coaligned crystals of Fe_xNbS_2 ($x = 0.32$–0.34) mounted in the $(HK0)$ scattering plane at $T = 2$ and 38 K. A dataset acquired at $T = 60$ K was subtracted as the background. The intensity is in the unit of counts per 3×10^4 monitor counts. (c),(d) Calculated diffraction patterns for given spin configurations. The details are described in the main text. Representative transverse (θ) and longitudinal ($\theta - 2\theta$) scans (dots) measured on one single crystal close to stoichiometric ratio with (e) $x = 0.34$ at BT7 and (f) $x = 0.33$ at SPINS with $T = 5$ K. The markers ○, ∇, Δ denote the data collected in the $(HK0)$, (HHL), $(H0L)$ scattering planes at BT7, and ◁, ▷ are used for the $(HK0)$ and (HHL) scattering planes at SPINS, compatible with the markers in Fig. 10. The horizontal bars denote the instrument Q resolutions. The solid lines are the results of the fits to a Gaussian line shape. The corresponding configurations of the collimations are written in the panel. Error bars in all figures represent one standard deviation.

magnetic peak at $\mathbf{Q_2} = (0.25, 0.5, 0)$ has comparable intensity with the peak at $\mathbf{Q_1} = (0.5, 0.5, 0)$ [Fig. 3(e)]. Both peaks have their full width at half maximum (FWHM) determined by the instrumental Q resolution, marked by horizontal bars in the plots. The θ scan with the crystal in the $(H0L)$ plane, equivalent to an L scan, displays also a resolution-limited peak [Fig. 3(e)], indicating three-dimensional long-range order even though the structures are lamellar. For the $x = 0.33$ sample the relative intensity of peaks between $\mathbf{Q_1}$ and $\mathbf{Q_2}$ [Fig. 3(f)] are dramatically different from that with $x = 0.34$, having more intensity related to $k_1 = (0.5, 0, 0)$. We also collected superlattice peaks at a series of reciprocal lattice positions, $(0.5, 0.5, L)$, by varying L. The intensity decreases gradually with increasing L value; the intensity following roughly the square of the magnetic form factor, manifesting the magnetic nature of the superlattice peaks.

To study the temperature evolution of the two magnetic phases, the intensities at peak position $\mathbf{Q_1}$ and $\mathbf{Q_2}$ were measured as a function of temperature for the two samples, as shown in Figs. 4(a) and 4(b). The magnetic peak intensities are scaled to comply with the integrated areas of the peaks measured from the motor scans, and normalized by the integrated area of the nuclear Bragg peak (110). The samples were measured in the $(HK0)$ scattering plane for these two plots. Both samples display the onsets of two magnetic transitions, consistent with the transition temperature anomalies observed in the bulk characterization measurements. The first transition is identified at $T_{N1} \sim 45$ K based on a guide to the eye. To extract the power law exponent 2β and T_{N2}, we assume a Gaussian distribution of transition temperatures within the bulk crystal in the power law function [51,52]:

$$\int_0^\infty \left(1 - \frac{T}{t_N}\right)^{2\beta} \frac{1}{\sqrt{2\pi}\sigma} e^{-(t_N - T_N)^2/2\sigma^2} dt_N. \qquad (1)$$

The fits provide the results $T_{N2} = 30(1)$ and 39.4(2) K with the thermal width of $\sigma = 4(1)$ and 1.5(3) K, and the power law exponent $2\beta = 0.20(7)$ and 0.23(2) for the $x = 0.33$ and 0.34 crystals, respectively. The values for 2β are close to that for the ideal 2D Ising model, $2\beta = 0.25$, although, because of the large spread in T_N, one should not over-interpret this result. Specifically, we cannot rule out a weakly first-order transition.

Interestingly, both nearly stoichiometric samples display an increase of the magnetic peak intensity at $\mathbf{Q_1}$ below T_{N1}, followed by a partial drop of the intensity below T_{N2}. This rules out the scenario that the stoichiometric sample is simply composed of partial under- and overintercalated regions; otherwise we should simply see two separated order parameter curves. This unusual feature is also

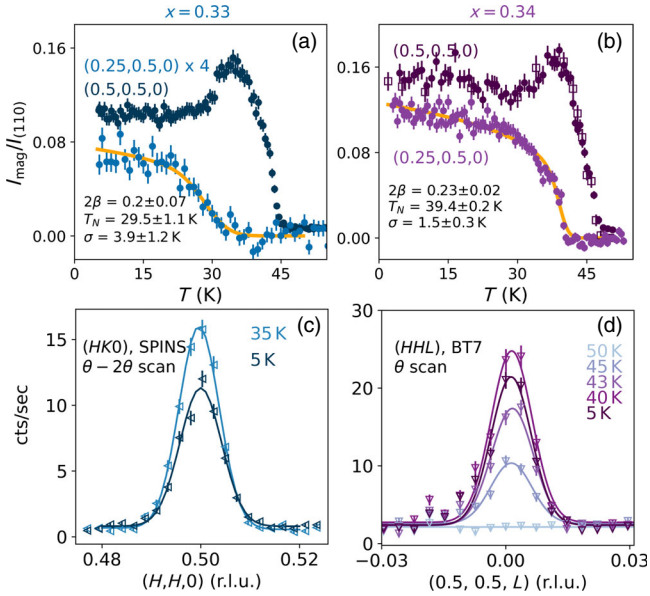

FIG. 4. Temperature dependence of the magnetic peak intensities at $\mathbf{Q_2} = (0.25, 0.5, 0)$ and $\mathbf{Q_1} = (0.5, 0.5, 0)$ for two nearly stoichiometric samples (a) $x = 0.33$ on SPINS and (b) $x = 0.34$ on BT7. The peak intensities are scaled to match the integrated intensities (empty squares) and both are normalized by the integrated intensity of the nuclear peak (110). Orange lines are the results of fits to the power law function with a thermal Gaussian distribution of T_N $[I \propto \int_0^\infty [1-(T/t_N)]^{2\beta} \times [1/(\sqrt{2\pi}\sigma)]e^{-(t_N-T_N)^2/2\sigma^2}dt_N]$ [51,52]. Representative motor scans at $\mathbf{Q_1}$ at elevated temperatures: (c) $\theta - 2\theta$ scan in the $(HK0)$ plane for $x = 0.33$ and (d) θ scan in (HHL) plane for $x = 0.34$. These correspond to in-plane and out-of-plane Q scans along the HH and L directions, respectively. The solid lines are the results of fits to a Gaussian function. Error bars in all panels represent one standard deviation.

confirmed in the $\theta - 2\theta$ and θ motor scans at elevated temperatures in Figs. 4(c) and 4(d). These measurements were carried out in the spectrometer configuration with the crystal mounted in the $(HK0)$ and (HHL) planes. Correspondingly, motor scans traversing across $\mathbf{Q_1}$ are equivalent to scans along the HH and L directions, respectively. The magnetic peaks at intermediate temperatures ($T = 35$ K in $x = 0.33$ and 40 K in $x = 0.34$) show higher intensities than the data at 5 K and a constant resolution-limited width from the Gaussian peak fits. These results preclude explanations due to the change of the magnetic correlations from 3D to 2D with decreasing temperature, which can lead to the broadening of the peak in the out-of-plane direction thereby reducing the peak intensity simultaneously within the plane.

2. Off-stoichiometric samples

To investigate the magnetic states and spin-glass-like physics in the off-stoichiometric samples, we measured two underintercalated samples ($x = 0.31$, 0.32) and one overintercalated sample ($x = 0.35$) in Fe_xNbS_2. The results turn out to be quite striking. In the $x = 0.32$ sample, we observed only magnetic peaks associated with wave vector $\mathbf{k_1}$, and no detectable peaks at the positions related to $\mathbf{k_2}$ [Figs. 5(a) and 5(c)]. In contrast, we observed only peaks associated with $\mathbf{k_2}$, not with $\mathbf{k_1}$, in the $x = 0.35$ sample [Figs. 5(b) and 5(d)]. The strongest intensity is observed at $\mathbf{Q_1} = (0.5, 0.5, 0)$ and $\mathbf{Q_2} = (0.25, 0.5, 0)$, respectively, for each sample. These peak positions were used to study the temperature-dependent behavior for each crystal.

The onset of the peaks at the two positions upon cooling clearly manifests magnetic transitions. (Fig. 6). From fits to the Gaussian-broadened power law function [Eq. (1)], we obtain T_N of 34.2(1) and 38.8(1) K with widths σ of 1.9(2) and 1.3(2) K, and power law exponents 2β of 0.20(2) and 0.21(2) for the $x = 0.32$ and 0.35 samples, respectively. The transition temperature in the $x = 0.32$ crystal is consistent with the second kink of χ_{ab} [see Fig. 15(c) in the Appendix]. While in $x = 0.35$, the transition temperature coincides with the peak anomaly in the susceptibility measurement [40]. The extracted values of the power law exponents, as well as for the stoichiometric sample, are consistent with the value for the 2D Ising system ($2\beta = 0.25$) [53,54] as we noted previously.

The width of the magnetic Bragg peaks in both samples agrees within the measurement uncertainties with the instrumental resolution, thence implying long-range AFM order. Naively, this might be seen to be unexpected since the magnetization measurements manifest a bifurcation between the ZFC and FC processes and a slow relaxation of the magnetization. Specifically, we might

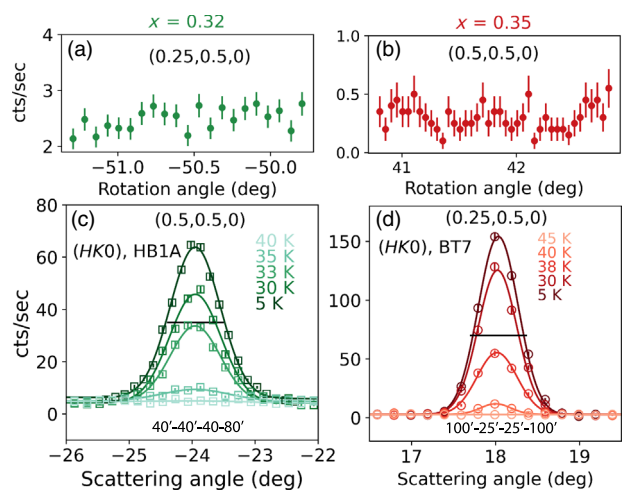

FIG. 5. Sample rotation θ scans at the given positions at $T = 5$ K for (a) $x = 0.32$ and (b) $x = 0.35$, showing no detectable signals. Representative temperature-dependent $\theta - 2\theta$ scans for (c) $x = 0.32$ at $\mathbf{Q_1} = (0.5, 0.5, 0)$ and (d) $x = 0.35$ at $\mathbf{Q_2} = (0.25, 0.5, 0)$. The solid lines are results of fits to the Gaussian function with the resolution shown in the horizontal black line at 5 K.

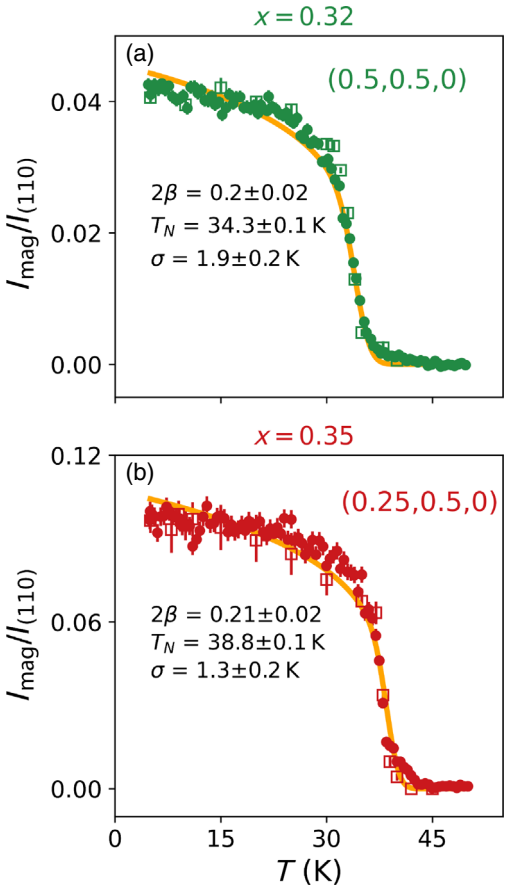

FIG. 6. Temperature dependence of the magnetic peak intensity (filled dots) for (a) underintercalated sample $x = 0.32$ at $\mathbf{Q_1} = (0.5, 0.5, 0)$ on HB1A and (b) overintercalated sample $x = 0.35$ at $\mathbf{Q_2} = (0.25, 0.5, 0)$ on BT7. Empty squares are integrated intensities extracted from the Gaussian fits to the $\theta - 2\theta$ scans in Fig. 5. Orange lines are the results of fits to the power law function with a Gaussian distribution of T_N [51].

have expected to observe a short-ranged magnetically ordered state in light of the apparent spin-glass behavior.

In the $x = 0.31$ crystal, we examined scans along the high symmetry directions and also carried out a 2D mapping in $(HK0)$ plane at 5 K on SPINS. To our surprise, we found no short- or long-ranged magnetic signal above the background level below T_f or T_N. This could be due to the in-plane disorder that destroys magnetic order, or that the magnetic signals were sufficiently broad that they could not be distinguished from the background.

3. Field-cooled neutron scattering measurements

We also employed neutron diffraction measurements in the presence of an applied magnetic field at MACS on the coaligned crystals to investigate any relevant spin-glass behavior. Interestingly, we observed a broadening of the magnetic superlattice peak at wave vector $\mathbf{Q_1}$ by cooling the crystal across T_N under an 8 T (T) magnetic field. This

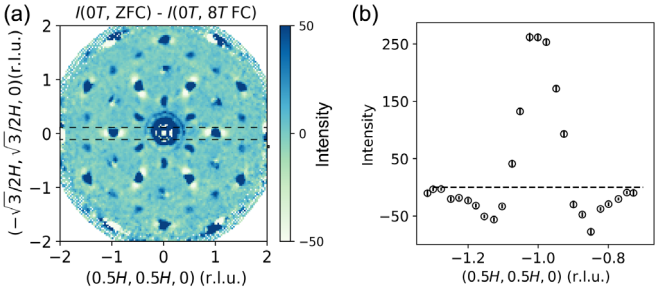

FIG. 7. (a) Single crystal neutron diffraction pattern in $(HK0)$ plane at 2 K with zero-field-cooled process, with data collected with cooling in an 8 T (T) magnetic field subtracted. The data were folded with sixfold rotational symmetry and expanded to the full rotation angle for presentation purposes. The intensity is in the unit of counts per 3×10^4 monitor counts. (b) The cut along $(0.5H, 0.5H, 0)$ with integrating the range of $H = [-0.07, 0.07]$ r.l.u. in $(-\sqrt{3}/2H, \sqrt{3}/2H, 0)$ direction, as marked by the dashed rectangle in (a). These are the data obtained by subtracting the 8 T field-cooled measurement. The dashed line denotes the base line with zero intensity in (b).

broadening is evident by viewing the diffraction pattern in a ZFC measurement with the pattern obtained after subtracting an equivalent FC measurement as shown in Fig. 7. The Q cut across the position of $(-0.5, -0.5, 0)$ in the difference pattern exhibits more intensity at the peak center and two symmetric wings with negative net counts after the subtraction [Fig. 7(b)]. That implies a different line shape of the magnetic peak in the FC process compared with the ZFC process. Such peak broadening on field cooling was also observed in other dilute two-dimensional Ising antiferromagnets [52,55], in which the broadening is attributed to the random staggered magnetic field generated by the applied magnetic field.

To sum up our single crystal neutron scattering measurements, we have obtained the following principal magnetic properties in Fe_xNbS_2 with varying intercalation ratio x but with identical crystallographic structures. (1) Strong magnetic intensities at in-plane positions suggesting that the spins are oriented along the c axis, consistent with the highly anisotropic magnetization data. (2) Two types of magnetic phases associated with wave vector $\mathbf{k_1} = (0.5, 0, 0)$ and $\mathbf{k_2} = (0.25, 0.5, 0)$ were observed. We observed magnetic peaks related to only $\mathbf{k_1}$ in samples with $x < 1/3$, both $\mathbf{k_1}$ and $\mathbf{k_2}$ in stoichiometric samples, $x \sim 1/3$, and $\mathbf{k_2}$ alone in overintercalated crystals, that is, $x > 1/3$. (3) In crystals with $x \sim 1/3$, there are two successive magnetic transitions, showing a rise-and-fall feature in the peak intensity curve. (4) All samples, except for the heavily underintercalated sample ($x = 0.31$), exhibit resolution-limited peaks implying long-range order within the given resolution. The fitted power law exponent β is consistent with 2D Ising behavior ($\beta = 0.125$) [54], although the uncertainties are large and we cannot rule out a weakly first-order transition due to the spread of the

transition temperature T_N. (5) No clear features related to spin-glass physics are evident from neutron diffraction measurements under zero field; however, magnetic peak broadening in the measurement with coaligned crystals presumably due to induced staggered random field effects was observed in the field-cooled process. We note that the dramatic changes in the magnetic structures as going from $x = 0.32$ to $x = 0.35$ necessitate that the crystals are homogeneous with variation of x of at most 0.01 within the samples.

C. Magnetic structure determination

For a systematic analysis of possible magnetic structures associated with $\mathbf{k_1}$ and $\mathbf{k_2}$, we use representation analysis in SARAh [56] and also BasIreps in FullProf [57], and calculate magnetic scattering intensities. Given the crystallographic symmetry $P6_322$, the $2c$ Wyckoff position for the Fe atoms, and propagation wave vector $\mathbf{k}$, group theory analysis describes that the magnetic representation Γ_{mag} can be decomposed into irreducible representations (IRs) and their corresponding basis vectors (BVs). According to Landau theory, the magnetic symmetry can be described by one IR for each transition. This information is then implemented to perform model calculations for the determination of the magnetic structure. For single crystal diffraction, the measured magnetic coherent cross section follows the expression [58]:

$$\frac{d\sigma}{d\Omega} = N_M \frac{(2\pi)^3}{V_M} p^2 \sum_{\mathbf{G}_M} \delta(\mathbf{Q} - \mathbf{G}_M) |\mathbf{F}_\perp(\mathbf{Q})|^2. \quad (2)$$

Here $|\mathbf{F}_\perp(\mathbf{Q})|^2 = |\mathbf{F}_M(\mathbf{Q})|^2 - |\hat{\mathbf{e}} \cdot \mathbf{F}_M(\mathbf{Q})|^2$ contains the static magnetic structure factor and magnetic form factor and represents the component of the spin axis perpendicular to $\mathbf{Q}$. $\mathbf{G}_M$ is the wave vector transfer associated with the reciprocal lattice vector $\boldsymbol{\tau}$ as $\mathbf{G}_M = \boldsymbol{\tau} \pm \mathbf{k}$ and a single propagation vector $\mathbf{k}$. N_M and V_M are the number and volume of the magnetic unit cell, respectively, and $p = 2.695$ fm. The magnetic structure factor $\mathbf{F}_M$ is related to the spin configuration as

$$\mathbf{F}_M(\mathbf{Q}) = \sum_j f(\mathbf{Q}) \mathbf{S}_{\mathbf{k},j} e^{i\mathbf{Q}\cdot\mathbf{r}_j}, \quad (3)$$

where $\mathbf{S}_{\mathbf{k},j}$ is the spin moment for atom j at the position r_j within a magnetic unit cell, and can be written by the BVs in irreducible representation analysis. By this formalism we can calculate magnetic scattering intensities for different spin structures and determine the configuration most accordant with the data.

First, we describe the representation analysis for the two types of propagation vectors $\mathbf{k_1}$ and $\mathbf{k_2}$ and discuss the choice of BVs supported by the observed data.

1. Phase $\mathbf{k_1} = (0.5,0,0)$

For the propagation vector $\mathbf{k_1} = (0.5, 0, 0)$, the magnetic representation Γ_{mag} can be decomposed into IRs $\Gamma_{\mathrm{mag}} = \Gamma_1 + 2\Gamma_2 + 2\Gamma_3 + \Gamma_4$ with corresponding BVs listed in Table I. Because the moment direction has been determined to be predominantly along the c axis by both the magnetic susceptibility and neutron data, only Γ_2 (ψ_2, ψ_3) and Γ_3 (ψ_4, ψ_5) are relevant. For the same reason, we concentrate on the BV ψ_3 and ψ_5. The difference between them is two Fe atoms in one unit cell [Fig. 1(a)] oriented parallel or antiparallel, respectively. The calculated magnetic scattering patterns [Fig. 3(d) and Fig. 16 in the Appendix] with ψ_5 agree with the data, showing an antiparallel stacking between two Fe spins. This is consistent with the strongest intensity being observed at $\mathbf{Q_1} = (0.5, 0.5, 0)$. Though ψ_4 is also allowed by group theory analysis, however, no peak feature is observed at the position $\mathbf{Q} = (0.5, 0.5, 1)$ [Fig. 3(e)] disfavoring the spin component related to that peak position, suggesting an absence of any measurable in-plane moment associated with $\mathbf{k_1}$.

The spin configuration corresponding to ψ_5 is shown in Figs. 8(a)–8(c). It consists of spins oriented in the same direction along one crystal axis and alternating along the other one, forming a stripe pattern elongated along an in-plane high symmetric crystal axis. Two Fe atoms with different c coordinates stack antiferromagnetically. We named this configuration "AFM stripe" for simplicity. The magnetic unit cell is 2 times the size of the structural unit cell. Note that there are three equivalent k vectors [(0.5,0,0), (0,0.5,0), and $(0.5, -0.5, 0)$], corresponding to three magnetic domains along three directions [Fig. 8(c)].

2. Phase $\mathbf{k_2} = (0.25,0.5,0)$

For the propagation vector $\mathbf{k_2} = (0.25, 0.5, 0)$, the magnetic representation Γ_{mag} decomposes into IRs $\Gamma_{\mathrm{mag}} = 3\Gamma_1 + 3\Gamma_2$ with corresponding BVs listed in Table II. Six BVs describe a collinear (ψ_2, ψ_3, ψ_5, ψ_6) and noncollinear (ψ_1, ψ_4) spin configuration. ψ_2 and ψ_6 depict two parallel Fe spins, while ψ_3 and ψ_5 represent

TABLE I. Basis vectors (BVs) ψ_i of IRs for two Fe atoms in the unit cell [Fe1, (0.333,0.667,0.25); Fe2, (0.667,0.333,0.75)] associated with propagation vector $\mathbf{k_1} = (0.5, 0, 0)$. BVs are defined by the crystallographic axes.

IR	BV	Fe1	Fe2
Γ_1	ψ_1	(2 1 0)	(−2 −1 0)
Γ_2	ψ_2	(0 −1 0)	(0 1 0)
	ψ_3	(0 0 1)	(0 0 1)
Γ_3	ψ_4	(0 −1 0)	(0 −1 0)
	ψ_5	(0 0 1)	(0 0 −1)
Γ_4	ψ_6	(2 1 0)	(2 1 0)

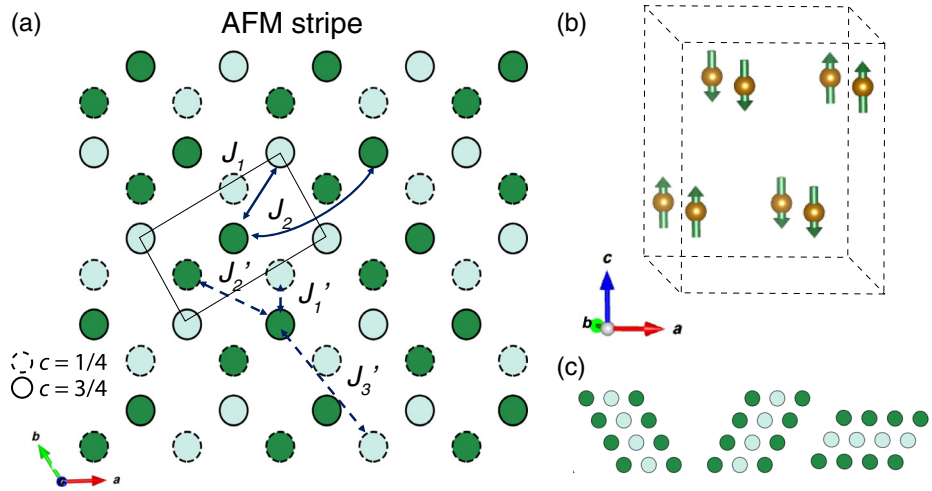

FIG. 8. AFM stripe magnetic structure associated with the $\mathbf{k_1} = (0.5, 0, 0)$ domain in Fe_xNbS_2 ($x < 1/3$): view in (a) ab plane and (b) three dimensions. AFM in the notation for the spin configuration is defined when two Fe atoms in one unit cell have antiparallel spins. Circles with solid and dashed outlines in (a) represent two Fe layers at $c = 3/4$ and $c = 1/4$. Dark and light colors denote spins up and down. Solid rectangle depicts the smallest magnetic unit cell. (c) Plots of three equivalent domain directions within one Fe triangular lattice layer.

antiparallel spins in one unit cell. By qualitatively comparing these to the diffraction pattern associated with $\mathbf{k_2}$ [Fig. 3(a)], the calculated patterns [Fig. 3(c) and Fig. 17 in the Appendix] that are described by ψ_3 and ψ_5 clearly follow selection rules for the magnetic peaks that are consistent with the observation. The other BVs result in unwanted reflections, for example, $\mathbf{Q} = (0.25, 0.25, 0)$.

The corresponding spin configuration is displayed in Figs. 9(a)–9(c). The difference between ψ_3 and ψ_5 is spin moments directed out of plane and in plane, respectively. Within the layer, spins point in the sequence of $++--$ along one crystal axis ($+$ and $-$ denote spins up and down for ψ_3). Two Fe atoms in one unit cell have spins pointing in opposite directions. Since connecting the same direction of the Fe spins within one layer institutes a zigzag route, we named this configuration "AFM zigzag" for simplicity. The minimum magnetic unit cell is 4 times the structural unit cell, and orthohexagonal. Note that there are six equivalent k vectors [(0.5,0.25,0), $(0.5, -0.75, 0)$, $(0.75, -0.25, 0)$, (0.25,0.5,0), $(-0.75, 0.5, 0)$, and $(-0.25, 0.75, 0)$], leading to three magnetic domains along three directions [Fig. 9(c)].

TABLE II. Basis vectors ψ_i of IRs for two Fe atoms in unit cell [Fe1, (0.333,0.667,0.25); Fe2, (0.667,0.333,0.75)] associated with propagation vector $\mathbf{k_2} = (0.25, 0.5, 0)$. BVs are defined by the crystallographic axes.

IR	BV	Fe1	Fe2
Γ_1	ψ_1	$(1\ \ 0\ \ 0)$	$(-i\ \ -i\ \ 0)$
	ψ_2	$(0\ \ 1\ \ 0)$	$(0\ \ i\ \ 0)$
	ψ_3	$(0\ \ 0\ \ 1)$	$(0\ \ 0\ \ -1)$
Γ_2	ψ_4	$(1\ \ 0\ \ 0)$	$(i\ \ i\ \ 0)$
	ψ_5	$(0\ \ 1\ \ 0)$	$(0\ \ -i\ \ 0)$
	ψ_6	$(0\ \ 0\ \ 1)$	$(0\ \ 0\ \ i)$

Next, we quantitatively determine the magnetic structures for off and nearly stoichiometric Fe_xNbS_2 samples.

3. Spin structure

The neutron scattering data for the off-stoichiometric samples display a single magnetic transition with wave vector $\mathbf{k_1}$ and $\mathbf{k_2}$ in the $x = 0.32$ and $x = 0.35$ crystals, respectively. In the $x = 0.32$ sample, since the strongest peak in the $(HK0)$ plane is at $\mathbf{Q} = (0.5, 0.5, 0)$, the spin structure with spins along the c axis is described by the basis vector of ψ_5 in the irreducible representation Γ_3 (Table I). The ordered moment was obtained as $m = 2.6(3)\mu_B$ from comparison between the observed and calculated intensities [Fig. 10(c)] by using Eqs. (2) and (3) and a normalization factor from the nuclear peaks. The spin configuration can be described as AFM stripe with the moments oriented along the c axis [Fig. 8(b)].

In the overintercalated $x = 0.35$ sample, all of the magnetic reflections are related to the wave vector $\mathbf{k_2}$. Since only one IR is allowed for a second-order phase transition, ψ_3 in Γ_1 (Table. II) was assigned to provide consistent results with the observed magnetic intensities [Fig. 10(e)]. The ordered moment was obtained as $m = 3.0(3)\mu_B$, and the spin configuration can be described as AFM zigzag with moments along c axis [Fig. 9(b)].

Nearly stoichiometric samples with $x \sim 1/3$ have two magnetic transitions. Below T_{N1}, the spin structure can be ascribed to the AFM stripe configuration [Fig. 8(b)] depicted by ψ_5 in Γ_3 with ordered moment of $2.9(3)\mu_B$ [Fig. 10(a)]. Below T_{N2}, to elaborate the rise-and-fall

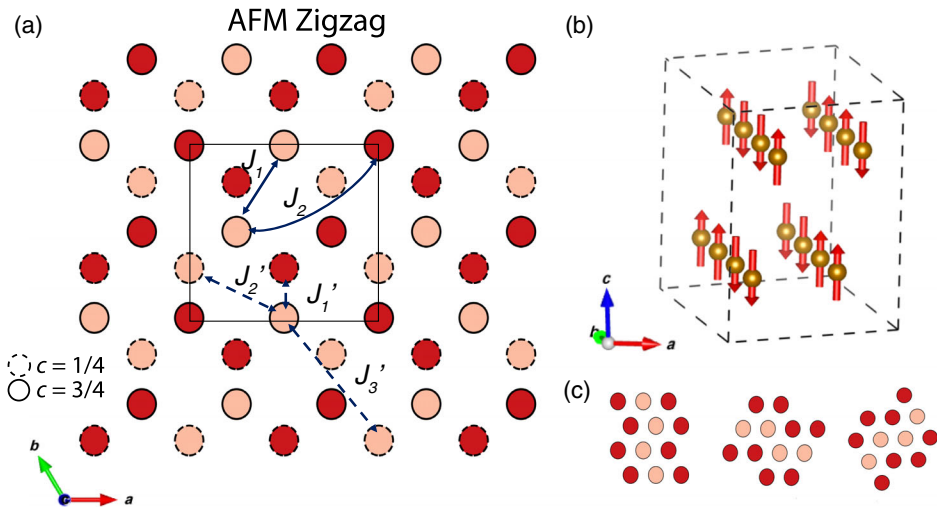

FIG. 9. AFM zigzag magnetically ordered phase associated with the $\mathbf{k_2} = (0.5, 0.25, 0)$ domain in Fe_xNbS_2 ($x > 1/3$): view in (a) *ab* plane and (b) three dimensions. AFM in the notation for the spin configuration is defined when two Fe atoms in one unit cell have antiparallel spins. Circles with solid and dashed outlines in (a) represent two Fe layers at $c = 3/4$ and $c = 1/4$. Dark and light colors denote spins up and down. Solid rectangle depicts the smallest magnetic unit cell. (c) Plots of three equivalent domain directions within one Fe triangular lattice layer.

feature of magnetic peak at $\mathbf{Q_1} = (0.5, 0.5, 0)$ and the second phase transition, one possible scenario is to assign in-plane component associated with zigzag configuration (Table II: ψ_5 in Γ_2), which is allowed by the group theory and IR analysis. However, the calculated tilting angle (see the Appendix) contradicts the large *c*-axis magnetic

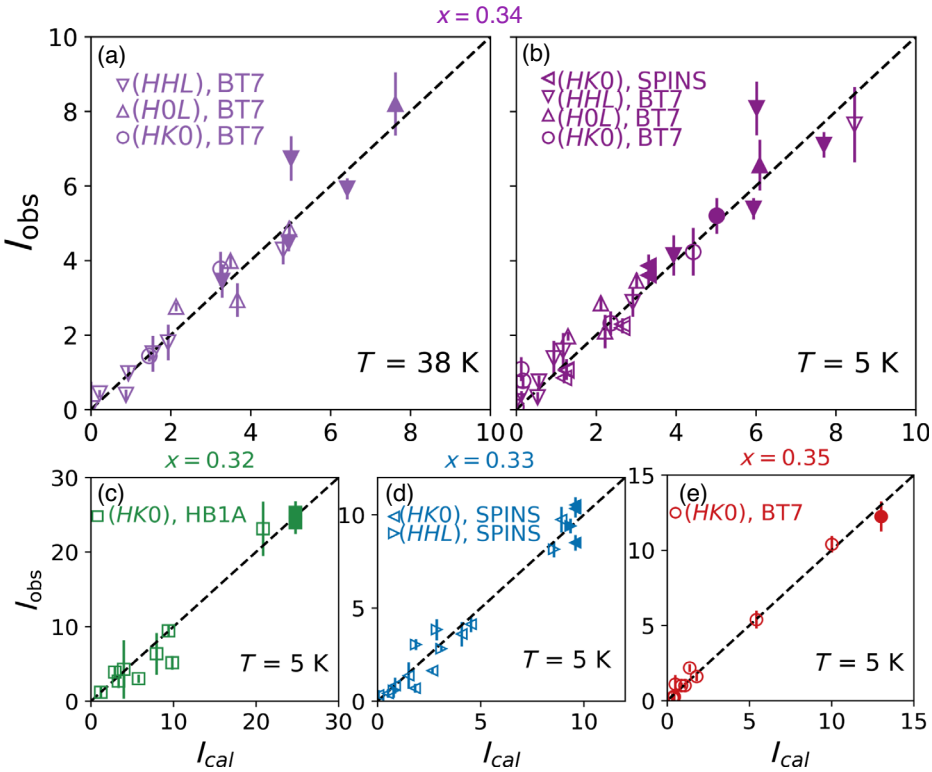

FIG. 10. Observed versus calculated intensities of nuclear (filled symbols) and magnetic (empty symbols) peaks at $T = 38$ K (a) and 5 K (b) for Fe_xNbS_2 crystal with $x = 0.34$, (c) $x = 0.32$, (d) $x = 0.33$, and (e) $x = 0.35$. Symbols in different types are data collected in different scattering planes and instruments according to the legends in each panel. The calculated and observed intensities of peaks under different scattering geometries have been scaled simultaneously in order to be presented within the same frame.

anisotropy found in our susceptibility measurements and, furthermore, would require a DM interaction orders of magnitude larger than that allowed for by theory.

Alternatively, the rise-and-fall feature can be viewed as simply the zigzag phase developing at the expense of the stripe phase. This can readily occur with decreasing temperature when the energy of two magnetic phases is nearly degenerate and the relative energies of the two phases change subtly as a function of temperature. That is, the delicate energy balance between the two phases changes around T_{N2} so that increasing regions of the sample favor the zigzag phase as the temperature is decreased. This can also happen if, as the zigzag phase grows, the domain boundaries of the stripe phase are converted to the zigzag configuration. Real space imaging of the domains would help elucidate this growth process. The redistribution of two magnetic phases is consistent with the rounding of the T_N [Figs. 4(a) and 4(b)], indicating a small spread in the Fe ratio across the sample. In this scenario, the calculated intensities with ratio of ~75% and ~35% stripe phase for $x = 0.33$ and $x = 0.34$ samples, respectively, are consistent with the observed patterns [Figs. 10(b) and 10(d)] at 5 K. The ordered moment is extracted as $3.2(3)\mu_B$ and $3.5(3)\mu_B$ correspondingly. The smaller value of these moments from the saturated moment under high field (~$4\mu_B$ per Fe) is likely due to errors in the normalization factor because of the limited number of nuclear Bragg peaks.

In summary, the sample with measured $x = 0.32$ shows a pure stripe magnetic phase, the samples with $x = 0.33$ and 0.34 show mixed phases, and the sample with $x = 0.35$ shows a pure zigzag phase. This suggests that the crossover from the stripe to the zigzag phase occurs at $x = 1/3$. The subtle change of Fe ratio surprisingly results in a rapid change of magnetic ground states, as well as the spintronic response. Next, we discuss these findings and relations between the two.

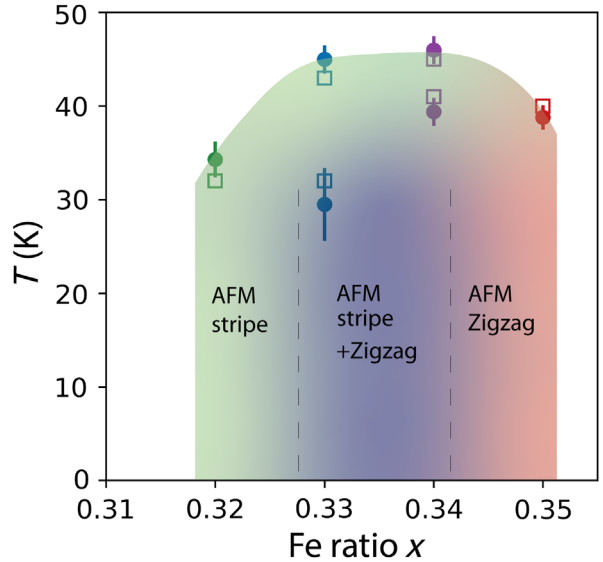

FIG. 11. Schematic phase diagram as a function of Fe ratio x around the critical value of $1/3$. This reveals a rapid change of magnetic phases from a single stripe order (green) in $x < 1/3$, across the coexisted two magnetic phases (purple) in $x \sim 1/3$, to a pure zigzag order (red) in $x > 1/3$. The solid dots denote the extracted transition temperatures from the neutron scattering measurements. The empty squares are characteristic temperatures of T_N (or T_f) from the magnetization measurements guided to the eyes. The dashed lines are imaginary phase boundaries. For $x = 0.31$, we do not observe any detectable magnetic signal.

IV. DISCUSSIONS

A. Highly degenerate magnetic phases

In general, one finds that magnetic defects typically suppress transition temperatures and reduce magnetic correlations. Here, both the ordered moments and transition temperatures are slightly reduced for off-stoichiometric samples. The remarkable observation here is the dramatic difference in the spin structures tuned by a small change in the concentration and the nature of the magnetic defects, namely from vacancies at the $2c$ site to interstitials (possibly at the $2d$ or $2b$ sites). As shown in the schematic phase diagram (Fig. 11), our single crystal neutron diffraction measurements reveal that the spin structure changes from purely stripe to purely zigzag by varying δ from ~ -0.01 to 0.02 with both phases coexisting in near-stoichiometric samples. We should emphasize that the two distinct spin structures reveal a totally different in-plane spin configuration, which is uncommon in lamellar structures. These results demonstrate the first example of flexible tuning of the magnetic ground state by a subtle change of magnetic defects in the intercalation complexes of the Nb and Ta dichalcogenides and, more generally, a rare example in magnetic vdW compounds.

In the noncentrosymmetric intercalation species, several characteristic magnetic interactions are relevant. Two anisotropic exchange interactions are considered in $Fe_{1/3+\delta}NbS_2$. First, single-ion anisotropy and, possibly, anisotropic exchange (~2 meV) result in highly anisotropic uniaxial Ising behavior, distinct from the easy-plane anisotropy observed in other T_xNbS_2 species studied so far [14]. Second, the Dzyaloshinskii-Moriya antisymmetric interaction originates from the loss of inversion symmetry. Specifically, the interlayer DM interactions with an in-plane component [59] could theoretically produce a small in-plane moment. Unfortunately, the extreme sensitivity of the magnetic ground state to the Fe concentration makes the determination of any small tilt angle of the spins indicated by zero-field anisotropic magnetoresistance (ZFAMR) measurement [40] extremely difficult.

Both the Ruderman-Kittel-Kasuya-Yosida interaction and the superexchange interaction were considered as the relevant mechanisms for the magnetic ordering in this

system [13,14]. The former is long-ranged and variable in both sign and magnitude; it relies on the separation of localized moments and the Fermi wave vector [60–62]. The latter is relatively short-ranged and the sign and magnitude are often determined by application of the Goodenough-Kanamori rules [63,64]. Since two dramatically different ordered phases are facilitated by a small concentration of magnetic defects, the superexchange interaction would be barely affected without a change of the local structure. Alternatively, the change of magnetic defects from vacancies to interstitials, presumably, could influence the RKKY interaction, especially for the interlayer exchange coupling with its larger Fe-Fe distance. This scenario is embedded in the oscillatory character of RKKY interaction [60–62,65,66]; it is analogous to the alternating exchange couplings in transition-metal layers separated by a nonmagnetic metal spacer [67,68].

Recent density functional theory studies [47,69] of the AFM stripe and AFM zigzag magnetic ground states strongly support our experimental results. To partially account for enhanced localizations of Fe d electrons, a Hubbard U correction was added in the DFT calculations. Both $U = 0.3$ eV and $U = 0.9$ eV predict an easy-axis anisotropy along [001], consistent with experiment. PBE $+ U$ energies for magnetic orderings corresponding to AFM stripe [$\mathbf{k}_1 = (0.5, 0, 0)$] and AFM zigzag [$\mathbf{k}_2 = (0.25, 0.5, 0)$] are reported to differ in energy by at most a few (1–3) meV per Fe atom. For context, this energy scale is significantly smaller (2 meV$/k_B = 23.2$ K) than the onset temperature of either magnetic phase for near-stoichiometry samples, rendering the stripe and zigzag phases effectively degenerate. Moreover, intriguingly, the relative energy ordering of AFM stripe and AFM zigzag phases switches in going from PBE $+ U$ with $U = 0.3$ eV to $U = 0.9$ eV [47]. The AFM stripe is lower in energy by 0.9 meV/Fe by using $U = 0.3$ eV, whereas the AFM zigzag is lower by 2.5 meV/Fe by using $U = 0.9$ eV.

The near degeneracy and competition between AFM stripe and zigzag phases near stoichiometry can be further understood by a minimal Heisenberg model [47,69], neglecting the single-ion anisotropy since this contribution cancels when calculating differences in energy between [001] oriented collinear magnetic orders. We highlight the results of the prior work related to our experiments in what follows. The mean-field energy with classical spin S can be written as [47]

$$H = E_0 + \sum_{\langle ij\rangle} J_1 S^2 + \sum_{\langle\langle ij\rangle\rangle} J_2 S^2 + \sum_{\langle ij\rangle'} J_1' S^2 + \sum_{\langle\langle ij\rangle\rangle'} J_2' S^2 + \sum_{\langle\langle\langle ij\rangle\rangle\rangle'} J_3' S^2, \quad (4)$$

where one, two, and three pairs of brackets denote Heisenberg exchange constants between equivalent nearest, next-nearest, and third-nearest neighbor interactions, respectively, and the prime refers to interlayer interactions [Figs. 8(a) and 9(a)]. PBE $+ U$-derived Heisenberg exchange constants for both U values examined from Ref. [47] are given in meV per Fe atom in Table III. Based on the AFM nearest-neighbor interactions J_1 and J_1' alone, the mean-field energies for AFM stripe and zigzag are degenerate, and are primarily responsible for the antiferromagnetism within and between the layers in both structures. The degeneracy is broken by the relative small values of the next-nearest neighbor interactions J_2 and J_2' as well as third-nearest neighbor interlayer interaction J_3'. The energy difference between the two phases is $E_{\text{stripe}} - E_{\text{zigzag}} = 4J_2'S^2 - 4J_2S^2 - 8J_3'S^2$ [47]. The AFM stripe phase is then favored when $|J_2'| > |J_2| + 2|J_3'|$, whereas the AFM zigzag phase is energetically favored when $|J_2'| < |J_2| + 2|J_3'|$.

TABLE III. Heisenberg spin exchange constants, in meV/Fe atom, calculated with PBE $+ U$ for $U = 0.3$ eV and $U = 0.9$ eV. Positive values ($J > 0$) are AFM coupling constants in our notation, and negative ($J < 0$) couplings are FM. The prime refers to interplanar couplings.

	J_1	J_1'	J_2'	J_2	J_3'
$U = 0.3$ eV	+0.76	+0.49	−0.20	−0.006	−0.07
$U = 0.9$ eV	+0.57	+0.28	−0.16	−0.14	−0.09

The relative change in magnitude and even signs of three exchange constants can be attributed to the high degeneracy of the two magnetic phases. As a possible microscopic mechanism, we note that, on the one hand, the interlayer exchange interactions originated via RKKY mechanism are weak due to the long separation distance (∼9–10 Å) and further have an oscillatory nature. On the other hand, magnetic Fe defects that reside within or between layers can give rise to changes in the Fermi surface. Our preliminary photoemission work reveals a rapid change of the Fermi surface size from $x < 1/3$ to $x > 1/3$. This provides evidence that magnetic defects would affect the couplings between localized moments via the conduction electrons. Accordingly, the values or even sign of three exchange constants would be quite sensitive to x, leading to the tuning between the two AFM phases by magnetic defects from $x < 1/3$ to $x > 1/3$. As a result of the nearly degenerate states, the delicate balance of the two magnetic phases, which are spatially separated in the $x = 1/3$ sample, can be changed causing one phase to win over the other leading to the rise-and-fall feature in the order parameter curve. The knob could be subtle changes in the RKKY interactions with decreasing the temperature, or magnetoelastic interactions that would turn on when magnetic ordering sets in for the two different phases. Further calculations could elucidate the possible mechanisms. Also, highly degenerate states in the metallic bilayer triangular lattice would require more theoretical

modeling beyond that for the frustrated magnetism in the insulating single-layer triangular lattice Ising antiferromagnet [70–72].

B. Relation to the spintronic features

Magnetic defects not only tune the magnetic ground states, but they also influence the intriguing spintronic features in $Fe_{1/3+\delta}NbS_2$ [38,40]. By injecting a current pulse along the [100] direction, for $x < 1/3$ and $x > 1/3$ samples, the change in transverse resistance is positive and negative, respectively. In addition, the devices display more active responses in off-stoichiometric samples, either below or above the $x = 1/3$ sample, while for $x = 1/3$ the amplitude of the resistance switching is dramatically diminished. Our neutron work provides fundamental information on the magnetic ground states in samples with different Fe ratios that display rapid changes in the spintronic behaviors as a function of Fe concentrations.

First, in the $x < 1/3$ and $x > 1/3$ sample our neutron experiments clearly demonstrate single long-ranged stripe order and zigzag order, respectively, with both revealing three magnetic domains. These results provide important indications for some of the observed switching features. The observation of the change from stripe order to zigzag order directly corresponds to the reversal of the sign of the switching behaviors [Fig. 12(a), represented from Ref. [40]]. Both stripe and zigzag phase have three magnetic domains denoted as d_i $(i = 1, 2, 3)$. The orientation of each magnetic domain d_i is defined as along the direction of alternating spins. As shown in the conceptual pictures in Figs. 12(c) and 12(d), if one assumes that a current prefers a domain that is perpendicular to the applied current pulse via the Rashba coupling [73], pulse A (or B) will favor $d_2 + d_3$ (or d_1) domain in zigzag order [Fig. 12(c)] and d_1 (or $d_2 + d_3$) domain in stripe order [Fig. 12(d)]. This likely explains the opposite switching responses in identical device geometries, or in other words, under the same pulse current. Recent nonlocal switching experiments [74] reveal a change of switching behavior when populating another type of magnetic domains in a secondary spot of the crystal, consistent with this scenario.

Second, in the stoichiometric $x = 1/3$ sample, the evolution of the two magnetic phases is reflected in the response to electrical current and magnetic field where both the switching resistance and the ZFAMR reveal a sign change upon lowering the temperature [40]. The sign change upon cooling is consistent with the above speculations, where the balance between two magnetic phases will result in the preferences of different types of magnetic domains induced by currents across the two transitions. This is consistent with the calculation based on the current-induced repopulation of magnetic domains in the $x = 1/3$ sample [47]. In addition, the suppression of resistance

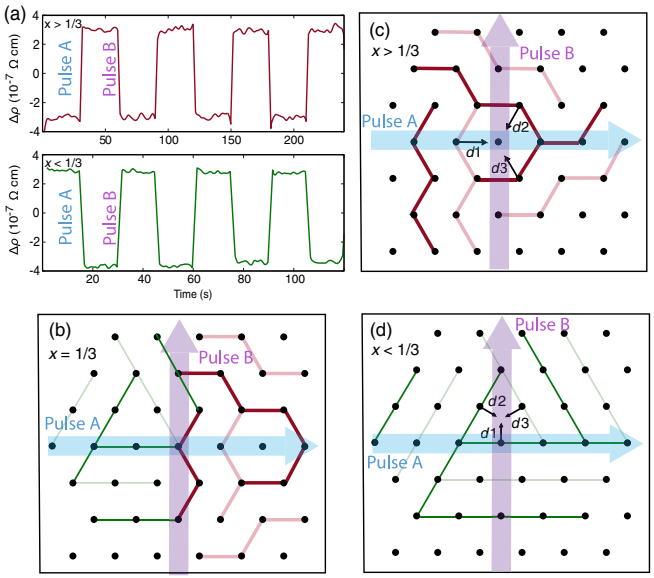

FIG. 12. (a) The change of resistance shows opposite signs between $x < 1/3$ and $x > 1/3$ samples given two orthogonal pulse currents A (blue) and (purple) (data from Ref. [40]). (b)–(d) Conceptual pictures to illustrate the possible scenario for the sign reversal of the switching resistance in the off-stochiometric samples as well as the suppressed magnitude in the $x = 1/3$ sample, based on determined single stripe in $x < 1/3$ and zigzag in $x > 1/3$ ordered phases, and coexistence of two phases in $x = 1/3$. For either stripe or zigzag phase, three magnetic domains are plotted in green or red colors, respectively. Dark and light colors denote spins up and down. Magnetic domain orientations (d_i with $i = 1, 2, 3$) are defined as the directions along alternating spins. By the same pulse A (or B), two single magnetic phases favor the populations of different domains. For detailed descriptions, see text.

switching with decreasing temperature and compared to the off-stochiometric samples could then be simply ascribed to the partial cancellation of the opposite resistance changes where two phases coexist [Fig. 12(b)]. Our specualtive ideas, however, require a detailed understanding of the actual switching mechanism both theoretically and experimentally, and this has not yet been definitively identified.

Finally, the apparent absence of AFM order in our heavily underintercalated sample ($x = 0.31$) is surprising. We do not observe any short-ranged magnetic peaks in our measurements that are typically associated with spin-glass order. Given the strong spin-glass-like feature in the susceptibility measurements and spin transport behaviors, it seems possible that dilute orphan spins might play a role in enhancing the switching effects, but further studies of samples in this regime by other experimental probes are required to understand the absent AFM order. In all, we provide empirical correlations between tunable magnetism and spintronic features, providing the foundation for more future work to decipher the mechanism.

V. CONCLUSIONS

To conclude, we have performed single crystal neutron diffraction experiments in the Fe intercalated transition-metal dichalcogenide material $Fe_{1/3+\delta}NbS_2$, which recently has been shown to exhibit intriguing resistance switching and magnetic memory effects. Two long-range ordered magnetic phases, specifically AFM stripe order with wave vector $k_1 = (0.5, 0, 0)$ and AFM zigzag order with $k_2 = (0.25, 0.5, 0)$, have been found and they can be sensitively tuned by the Fe concentration as one goes from the underintercatated to overintercaleted region of the phase diagram. This arises from the nearly degenerate energies for the two spin structures, supported by our DFT calculation. Two phases can be tuned from one to the other due to the oscillating nature of RKKY interaction J and the competition between secondary intra- and interlayer interactions. Two successive magnetic transitions are observed in stoichiometric samples; the emergence of the second magnetic phase is consistent with the remarkable near degeneracy in energy of the two states. We provide crucial information on magnetic ground states that form the basis for understanding the interesting spintronic behaviors. Our discovery of the highly tunable magnetic phases in this bulk sample open up new, intriguing opportunities to manipulate magnetic states and, concomitantly, the spintronic properties by magnetic defects.

ACKNOWLEDGMENTS

The authors would like to thank Edith Bourret-Courchesne, Didier Perrodin, Drew Onken, Peter Ercius, Rammamoorthy Ramesh, Yu He, Xiang Chen, Zhentao Wang, and Zhenglu Li for help and fruitful discussions. This work is partially funded by the U.S. Department of Energy, Office of Science, Office of Basic Energy Sciences, Materials Sciences and Engineering Division under Contract No. DE-AC02-05-CH11231 within the Quantum Materials Program (KC2202). The work of S. C. H., E. M., S. F. W., J. G. A., and J. B. N. was supported by the Center for Novel Pathways to Quantum Coherence in Materials, an Energy Frontier Research Center funded by the U.S. Department of Energy, Director, Office of Science, Office of Basic Energy Sciences under Contract No. DE-AC02-05CH11231. Access to MACS was provided by the Center for High Resolution Neutron Scattering, a partnership between the National Institute of Standards and Technology and the National Science Foundation under Agreement No. DMR-1508249. A portion of this research used resources at the High Flux Isotope Reactor, a U.S. DOE Office of Science User Facility operated by the Oak Ridge National Laboratory.

APPENDIX

This Appendix includes the following information: (1) details on the single crystal x-ray diffraction and energy dispersive spectroscopy measurements, (2) characterization of the other single crystals that were used in the neutron diffraction experiments, (3) remarks on the possibility of a small in-plane moment developed below T_{N2} in the $x = 1/3$ sample, and (4) the calculated pattern for each basis vector associated with $k_1 = (0.5, 0, 0)$ and $k_2 = (0.25, 0.5, 0)$.

1. Details on the XRD and EDX measurements

The single crystal x-ray measurement was performed in small crystals from the same batch of $x = 0.31$, 0.32, $1/3$, and 0.35 crystals as shown in Fig. 13. The images reveal three-dimensional Bragg peaks with no clear diffuse

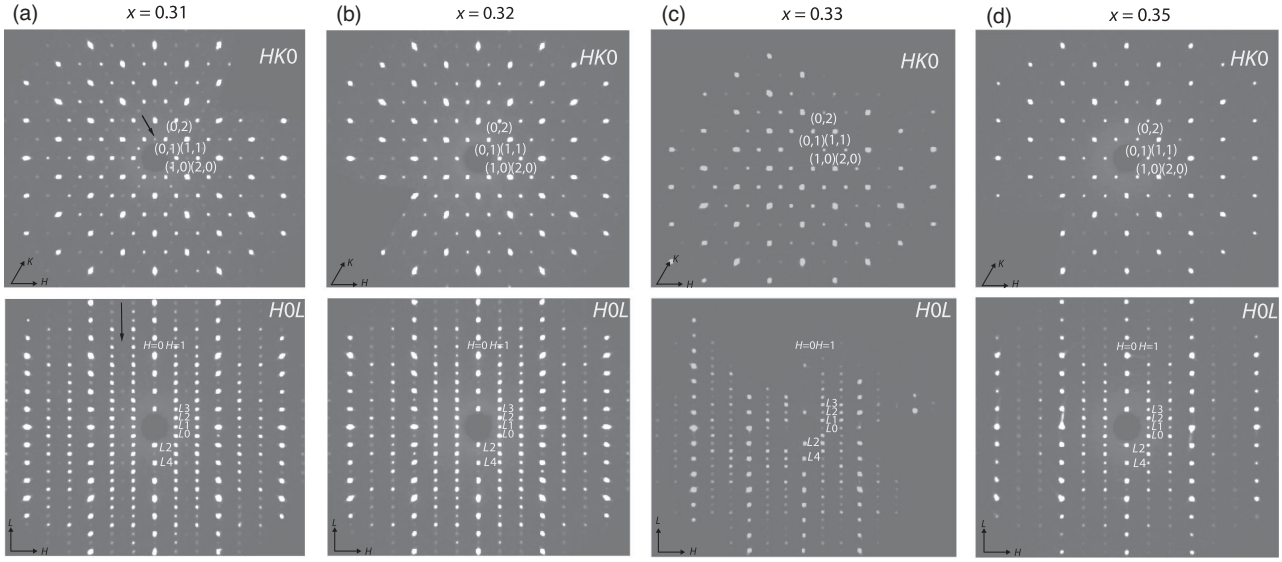

FIG. 13. Single crystal x-ray diffraction image in the $HK0$ and $H0L$ planes for $x = 0.31$ (a), 0.32 (b), $1/3$ (c), and 0.35 (d) crystals. $L1$ is short for $L = 1$, $L2$ for $L = 2$, etc. The black arrows denote the reflections associated with Fe occupying $2b$ sites.

TABLE IV. The atomic coordinates, the Wyckoff positions, lattice parameters, and goodness of fits R_1 from the single crystal structure refinements with the noncentrosymemtric space group $P6_322$ for four different intercalation ratios $x = 0.31$, 0.32, 1/3, and 0.35 from top to the bottom table. Occ. stands for the occupation number. We used Olex2 for the structural analysis.

Atoms	x	y	z	Site	Occ.
Fe1	2/3	1/3	0.25	$2c$	0.75
Fe2	0	0	0.25	$2b$	0.1
Nb1	0	0	0	$2a$	1
Nb2	1/3	2/3	0.001 03(3)	$4f$	1
S	0.331 50(13)	0.001 67(15)	0.370 68(12)	$12i$	1
$a = b = 5.7608(1)$ Å, $c = 12.1308(3)$ Å, $R_1 = 2.9\%$					

Atoms	x	y	z	Site	Occ.
Fe1	2/3	1/3	0.25	$2c$	0.855
Fe2	0	0	0.25	$2b$	0.045
Nb1	0	0	0	$2a$	1
Nb2	1/3	2/3	0.001 15(3)	$4f$	1
S	0.330 96(14)	0.001 91(16)	0.370 82(12)	$12i$	1
$a = b = 5.7614(1)$ Å, $c = 12.1436(3)$ Å, $R_1 = 3.11\%$					

Atoms	x	y	z	Site	Occ.
Fe1	2/3	1/3	0.25	$2c$	0.9
Fe2	0	0	0.25	$2b$	0.023
Nb1	0	0	0	$2a$	1
Nb2	1/3	2/3	0.001 21(2)	$4f$	1
S	0.330 63(9)	0.002 14(11)	0.370 80(8)	$12i$	1
$a = b = 5.7596(3)$ Å, $c = 12.1535(9)$ Å, $R_1 = 3.44\%$					

Atoms	x	y	z	Site	Occ.
Fe1	2/3	1/3	0.25	$2c$	0.96
Fe2	0	0	0.25	$2b$	0.063
Nb1	0	0	0	$2a$	1
Nb2	1/3	2/3	0.001 24(2)	$4f$	1
S	0.330 66(17)	0.002 35(9)	0.371 21(6)	$12i$	1
$a = b = 5.7597(2)$ Å, $c = 12.1914(4)$ Å, $R_1 = 1.59\%$					

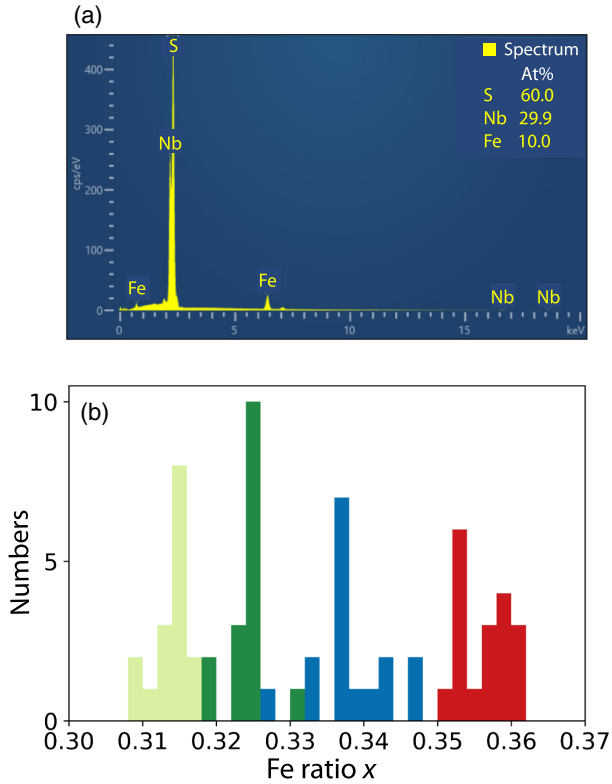

FIG. 14. (a) Representative energy dispersive spectroscopy spectrum in $x \sim 1/3$. At% stands for atomic ratio. (b) The histograms with binning size of 0.002 for Fe ratio x determined from the EDX analysis from the $x = 0.31$ (light green), $x = 0.32$ (green), $x \sim 1/3$ (blue), and $x = 0.35$ (red) sample. The standard deviation by measuring about 20 points is 0.003, 0.003, 0.005, and 0.003 for $x = 0.31$, 0.32, 0.33, and 0.35, respectively.

scattering signal along the L direction. A clear series of $(10L)$ peaks imply a minimal disorder [30]. The structures are well described by the noncentrosymemtric space group $P6_322$ with refined structures listed in the Table IV by using Olex2 structural analysis software. Additional weak series of peaks (marked by black arrows) are associated with the occupancy of Fe at $2b$ Wyckoff sites. Equally importantly, if alternative Fe sites occupy significantly, then the crossover from the stripe to zigzag magnetic phase for the $2c$ Wyckoff sites would by necessity occur at an overall Fe concentrations measurably higher than 1/3.

Energy dispersive x-ray spectroscopy measurements were performed to extract the iron intercalation ratio (Fig. 14). By detecting ~20 spots within the area of $100 \times 100\ \mu m^2$ for each sample, we measured the concentration of Fe, Nb, and S elements. We obtain the histogram for the value of x and averaged intercalation ratio x for our measured crystals. They are calculated to be $x = 0.31$, 0.32, 0.33, 0.34, and 0.35 given the EDX standard deviation of 0.003,0.003, 0.005,0.003. The estimated errors considering the factor from the instrument is up to ± 0.01 for our crystals. The more accurate ratio has been confirmed by inductively coupled plasma optical emission spectroscopy measurements [38].

2. Magnetization measurements

The magnetization measurements for the other measured neutron samples are shown in Fig. 15. The separation between the zero-field-cooled and field-cooled susceptibility is dependent upon the deviation from the stoichiometric ratio of 1/3. ZFC and FC curves separate at a characteristic temperature T_f; such a separation does not occur in samples with x very near 1/3. In the crystal with $x = 0.33$, the susceptibility along the c axis exhibits one anomalous peak followed by a broad hump with decreasing temperature; correspondingly, two kinks in the in-plane susceptibility χ_{ab} are shown at $T_{N1} \sim 32$ K and $T_{N2} \sim 43$ K. In the single crystal with $x = 0.32$, the second kink in χ_{ab}

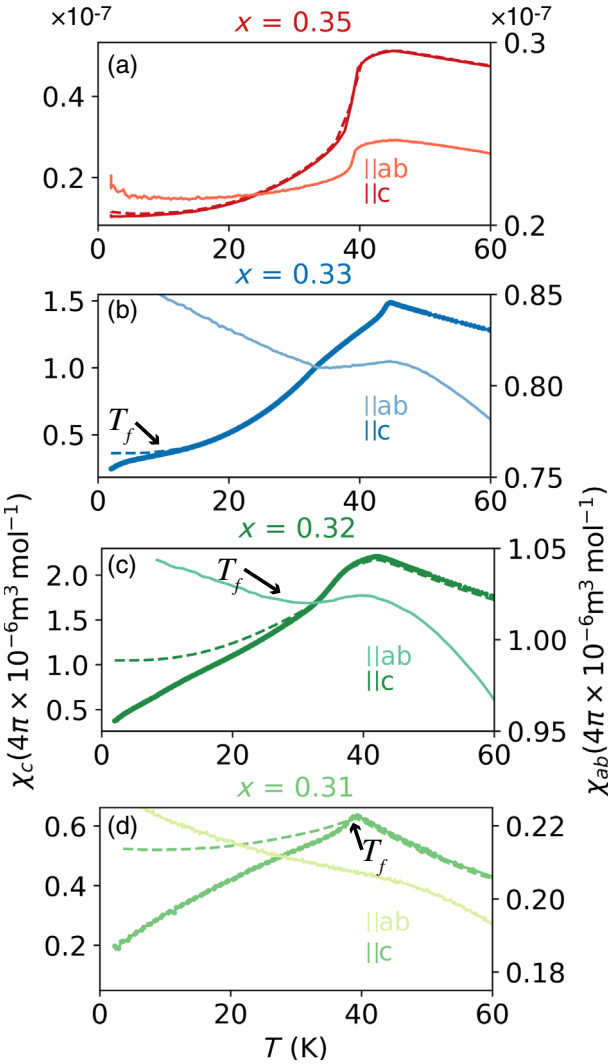

FIG. 15. Magnetization measurements for other compositions $x = 0.35$ (a), 0.33 (b), 0.32 (c), and 0.31 (d) with applied field of 0.1 T along c axis and in ab plane. The dashed and solid lines corresponding to the measurements with field-cooled and zero-field-cooled process.

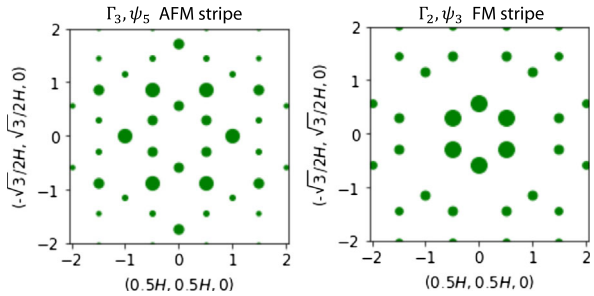

FIG. 16. Calculated intensities for given irreducible representation and basis vector associated with $\mathbf{k_1} = (0.5, 0, 0)$ and other two equivalent k's, describing a spin configuration of AFM stripe (left) and FM stripe (right) with moment direction along c axis. The size of dots represents the intensities of peaks, including contributions of all equivalent domains.

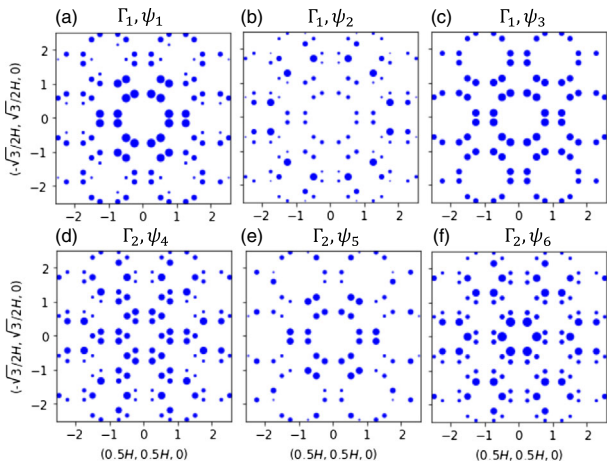

FIG. 17. Calculated intensities for given irreducible representation and basis vector associated with $\mathbf{k_2} = (0.5, 0.25, 0)$ and other five equivalent k's. Plots of (a)–(c) present the simulation for Γ_1 and (d)–(f) for Γ_2 IR, corresponding to the magnetic space group symmetry $P_c2_12_12$ and $P_c2_12_12_1$, respectively. The size of dots represents the intensities, including contributions of all equivalent domains.

occurs around $T_f \sim 32$ K. In the crystal with $x = 0.31$, T_f is close to the peak anomaly in the c-axis susceptibility around 40 K. In the $x = 0.35$ sample, the characterization data show the transition $T_N \sim 40$ K. Both off-stochiometric and stoichiometric samples exhibit strong uniaxial anisotropy in their susceptibilities (Fig. 2). For $x > 1/3$, Curie-Weiss fits to the susceptibility in the paramagnetic region yield values of the paramagnetic effective moment $\mu_{\mathrm{eff}} = 5.0(3)\mu_B$ and Curie-Weiss temperature $\theta_{\mathrm{CW}} = -50(2)$ K along the c axis; $\mu_{\mathrm{eff}} = 5.0(3)\mu_B$ and $\theta_{\mathrm{CW}} = -165(5)$ K in the ab plane. For $x < 1/3$, the Curie-Weiss fits in the paramagnetic region yield the values of paramagnetic effective moment $\mu_{\mathrm{eff}} = 5.0(3)\mu_B$ and Curie-Weiss temperature $\theta_{\mathrm{CW}} = -24(1)$ K along the c axis; $\mu_{\mathrm{eff}} = 4.7(2)\mu_B$ and $\theta_{\mathrm{CW}} = -104(2)$ K in the ab plane.

3. Remarks on the magnetic structure analysis

In the samples with $x \sim 1/3$ because of the complications presented by the coexistence of two different magnetic structures, it is not possible to say anything meaningful about any in-plane moment. However, any such in-plane moment would be caused by the interlayer DM interaction which is small compared to both the primary exchange and the c-axis anisotropy.

The single crystal neutron diffraction intensities are calculated according to Eqs. (2) and (3) in the main text. We utilize the BVs vector that describe the spin configuration and calculate the magnetic intensities. We derived the selection rule for each propagation wave vector as $\delta_{2h}\delta_k$ for the wave vector $\mathbf{k} = (0.5, 0, 0)$ domain, and $\delta_{2h}\delta_{h+2k}$ for the

wave vector $\mathbf{k} = (0.5, 0.25, 0)$ domain. Here h and k are Miller indices for the wave vector transfer Q. The calculation includes three domains with equal weights and the square of the magnetic form factor. The normalization factor for the magnetic peaks NC_m is obtained from the ratio between the calculated square of the structure factor and the integrated area of the nuclear peaks NC_n. The relation between them is $NC_m = [(N_n V_m)/(N_m * V_n)] * NC_n$, where V and N stand for the volume and number of magnetic (m) or nuclear (n) unit cell, respectively. By this normalization, we can obtain the ordered moment size by comparing the calculated and measured intensities as shown in Fig. 10.

[1] K. S. Burch, D. Mandrus, and J.-G. Park, *Magnetism in Two-Dimensional van der Waals Materials*, Nature (London) **563**, 47 (2018).

[2] J.-G. Park, *Opportunities and Challenges of 2D Magnetic van der Waals Materials: Magnetic Graphene?*, J. Phys. Condens. Matter **28**, 301001 (2016).

[3] P. Ajayan, P. Kim, and K. Banerjee, *Two-Dimensional van der Waals Materials*, Phys. Today **69**, No. 9, 38 (2016).

[4] C. Gong and X. Zhang, *Two-Dimensional Magnetic Crystals and Emergent Heterostructure Devices*, Science **363**, aav4450 (2019).

[5] K. F. Mak, J. Shan, and D. C. Ralph, *Probing and Controlling Magnetic States in 2D Layered Magnetic Materials*, Nat. Rev. Phys. **1**, 646 (2019).

[6] M. Gibertini, M. Koperski, A. F. Morpurgo, and K. S. Novoselov, *Magnetic 2D Materials and Heterostructures*, Nat. Nanotechnol. **14**, 408 (2019).

[7] T. Li, S. Jiang, N. Sivadas, Z. Wang, Y. Xu, D. Weber, J. E. Goldberger, K. Watanabe, T. Taniguchi, C. J. Fennie, K. Fai Mak, and J. Shan, *Pressure-Controlled Interlayer Magnetism in Atomically Thin* CrI_3, Nat. Mater. **18**, 1303 (2019).

[8] T. Song, Z. Fei, M. Yankowitz, Z. Lin, Q. Jiang, K. Hwangbo, Q. Zhang, B. Sun, T. Taniguchi, K. Watanabe, M. A. McGuire, D. Graf, T. Cao, J.-H. Chu, D. H. Cobden, C. R. Dean, D. Xiao, and X. Xu, *Switching 2D Magnetic States via Pressure Tuning of Layer Stacking*, Nat. Mater. **18**, 1298 (2019).

[9] M. J. Coak, D. M. Jarvis, H. Hamidov, A. R. Wildes, J. A. M. Paddison, C. Liu, C. R. S. Haines, N. T. Dang, S. E. Kichanov, B. N. Savenko, S. Lee, M. Kratochvílová, S. Klotz, T. C. Hansen, D. P. Kozlenko, J.-G. Park, and S. S. Saxena, *Emergent Magnetic Phases in Pressure-Tuned van der Waals Antiferromagnet* $FePS_3$, Phys. Rev. X **11**, 011024 (2021).

[10] C. R. S. Haines, M. J. Coak, A. R. Wildes, G. I. Lampronti, C. Liu, P. Nahai-Williamson, H. Hamidov, D. Daisenberger, and S. S. Saxena, *Pressure-Induced Electronic and Structural Phase Evolution in the van der Waals Compound* $FePS_3$, Phys. Rev. Lett. **121**, 266801 (2018).

[11] A. F. May, M.-H. Du, V. R. Cooper, and M. A. McGuire, *Tuning Magnetic Order in the van der Waals Metal* Fe_5GeTe_2 *by Cobalt Substitution*, Phys. Rev. Mater. **4**, 074008 (2020).

[12] G. Drachuck, Z. Salman, M. W. Masters, V. Taufour, T. N. Lamichhane, Q. Lin, W. E. Straszheim, S. L. Bud'ko, and P. C. Canfield, *Effect of Nickel Substitution on Magnetism in the Layered van der Waals Ferromagnet* Fe_3GeTe_2, Phys. Rev. B **98**, 144434 (2018).

[13] S. S. P. Parkin and R. H. Friend, *3d Transition-Metal Intercalates of the Niobium and Tantalum Dichalcogenides. I. Magnetic Properties*, Philos. Mag. B **41**, 65 (1980).

[14] R. H. Friend, A. R. Beal, and A. D. Yoffe, *Electrical and Magnetic Properties of Some First Row Transition Metal Intercalates of Niobium Disulphide*, Philos. Mag. **35**, 1269 (1977).

[15] J. Wilson, F. D. Salvo, and S. Mahajan, *Charge-Density Waves and Superlattices in the Metallic Layered Transition Metal Dichalcogenides*, Adv. Phys. **24**, 117 (1975).

[16] M. Naito and S. Tanaka, *Electrical Transport Properties in* $2H$-NbS_2, -$NbSe_2$, -TaS_2 *and* -$TaSe_2$, J. Phys. Soc. Jpn. **51**, 219 (1982).

[17] A. H. Castro Neto, *Charge Density Wave, Superconductivity, and Anomalous Metallic Behavior in 2D Transition Metal Dichalcogenides*, Phys. Rev. Lett. **86**, 4382 (2001).

[18] I. Guillamón, H. Suderow, S. Vieira, L. Cario, P. Diener, and P. Rodière, *Superconducting Density of States and Vortex Cores of* $2H$-NbS_2, Phys. Rev. Lett. **101**, 166407 (2008).

[19] K. T. Law and P. A. Lee, $1T$-TaS_2 *as a Quantum Spin Liquid*, Proc. Natl. Acad. Sci. U.S.A. **114**, 6996 (2017).

[20] A. Devarakonda, H. Inoue, S. Fang, C. Ozsoy-Keskinbora, T. Suzuki, M. Kriener, L. Fu, E. Kaxiras, D. C. Bell, and J. G. Checkelsky, *Clean 2D Superconductivity in a Bulk van der Waals Superlattice*, Science **370**, 231 (2020).

[21] F. Boswell, A. Prodan, W. R. Vaughan, and J. Corbett, *On the Ordering of Fe Atoms in* Fe_xNbS_2, Phys. Status Solidi A **45** (1978).

[22] F. Hulliger and E. Pobitschka, *On the Magnetic Behavior of New* $2H$-NbS_2*-Type Derivatives*, J. Solid State Chem. **1**, 117 (1970).

[23] K. Anzenhofer, J. Van Den Berg, P. Cossee, and J. Helle, *The Crystal Structure and Magnetic Susceptibilities of* $MnNb_3S_6$, $FeNb_3S_6$, $CoNb_3S_6$ *and* $NiNb_3S_6$, J. Phys. Chem. Solids **31**, 1057 (1970).

[24] Y. Togawa, T. Koyama, K. Takayanagi, S. Mori, Y. Kousaka, J. Akimitsu, S. Nishihara, K. Inoue, A. S. Ovchinnikov, and J. Kishine, *Chiral Magnetic Soliton Lattice on a Chiral Helimagnet*, Phys. Rev. Lett. **108**, 107202 (2012).

[25] D. Braam, C. Gomez, S. Tezok, E. V. L. de Mello, L. Li, D. Mandrus, H.-Y. Kee, and J. E. Sonier, *Magnetic Properties of the Helimagnet* $Cr_{1/3}NbS_2$ *Observed by* μSR, Phys. Rev. B **91**, 144407 (2015).

[26] Y. Kousaka, T. Ogura, J. Zhang, P. Miao, S. Lee, S. Torii, T. Kamiyama, J. Campo, K. Inoue, and J. Akimitsu, *Long Periodic Helimagnetic Ordering in* CrM_3S_6 *(*$M =$ Nb *and Ta)*, J. Phys. Conf. Ser. **746**, 012061 (2016).

[27] Y. Kousaka, Y. Nakao, J. Kishine, M. Akita, K. Inoue, and J. Akimitsu, *Chiral Helimagnetism in* $T_{1/3}NbS_2$ *(*$T =$ Cr *and Mn)*, Nucl. Instrum. Methods Phys. Res., Sect. A **600**, 250 (2009).

[28] S. K. Karna, F. N. Womack, R. Chapai, D. P. Young, M. Marshall, W. Xie, D. Graf, Y. Wu, H. Cao, L. DeBeer-Schmitt, P. W. Adams, R. Jin, and J. F. DiTusa, *Conse-*

quences of Magnetic Ordering in Chiral $Mn_{1/3}Nbs_2$, Phys. Rev. B **100**, 184413 (2019).

[29] S. S. P. Parkin, E. A. Marseglia, and P. J. Brown, *Magnetic Structure of* $Co_{1/3}NbS_2$ *and* $Co_{1/3}TaS_2$, J. Phys. C **16**, 2765 (1983).

[30] K. Lu, D. Sapkota, L. DeBeer-Schmitt, Y. Wu, H. B. Cao, N. Mannella, D. Mandrus, A. A. Aczel, and G. J. MacDougall, *Canted Antiferromagnetic Order in the Monoaxial Chiral Magnets* $V_{1/3}TaS_2$ *and* $V_{1/3}NbS_2$, Phys. Rev. Mater. **4**, 054416 (2020).

[31] A. A. Aczel, L. M. Debeer-Schmitt, T. J. Williams, M. McGuire, N. Ghimire, L. Li, and D. Mandrus, *Extended Exchange Interactions Stabilize Long-Period Magnetic Structures in* $Cr_{1/3}NbS_2$, Appl. Phys. Lett. **113**, 032404 (2018).

[32] A. E. Hall, D. D. Khalyavin, P. Manuel, D. A. Mayoh, F. Orlandi, O. A. Petrenko, M. R. Lees, and G. Balakrishnan, *Magnetic Structure Investigation of the Intercalated Transition Metal Dichalcogenide* $V_{1/3}NbS_2$, Phys. Rev. B **103**, 174431 (2021).

[33] Y. Togawa, T. Koyama, Y. Nishimori, Y. Matsumoto, S. McVitie, D. McGrouther, R. L. Stamps, Y. Kousaka, J. Akimitsu, S. Nishihara, K. Inoue, I. G. Bostrem, V. E. Sinitsyn, A. S. Ovchinnikov, and J. Kishine, *Magnetic Soliton Confinement and Discretization Effects Arising from Macroscopic Coherence in a Chiral Spin Soliton Lattice*, Phys. Rev. B **92**, 220412(R) (2015).

[34] N. J. Ghimire, A. S. Botana, J. S. Jiang, J. Zhang, Y. S. Chen, and J. F. Mitchell, *Large Anomalous Hall Effect in the Chiral-Lattice Antiferromagnet* $CoNb_3S_6$, Nat. Commun. **9**, 3280 (2018).

[35] R. Aoki, Y. Kousaka, and Y. Togawa, *Anomalous Nonreciprocal Electrical Transport on Chiral Magnetic Order*, Phys. Rev. Lett. **122**, 057206 (2019).

[36] O. Gorochov, A. L. Blanc-soreau, J. Rouxel, P. Imbert, and G. Jehanno, *Transport Properties, Magnetic Susceptibility and Mössbauer Spectroscopy of* $Fe_{0.25}NbS_2$ *and* $Fe_{0.33}S_2$, Philos. Mag. B **43**, 621 (1981).

[37] Y. Yamamura, S. Moriyama, T. Tsuji, Y. Iwasa, M. Koyano, S. Katayama, and M. Ito, *Heat Capacity and Phase Transition of* Fe_xNbS_2 *at Low Temperature*, J. Alloys Compd. **383**, 338 (2004).

[38] E. Maniv, R. A. Murphy, S. C. Haley, S. Doyle, C. John, A. Maniv, S. K. Ramakrishna, Y.-L. Tang, P. Ercius, R. Ramesh, A. P. Reyes, J. R. Long, and J. G. Analytis, *Exchange Bias due to Coupling between Coexisting Antiferromagnetic and Spin-Glass Orders*, Nat. Phys. **17**, 525 (2021).

[39] N. L. Nair, E. Maniv, C. John, S. Doyle, J. Orenstein, and J. G. Analytis, *Electrical Switching in a Magnetically Intercalated Transition Metal Dichalcogenide*, Nat. Mater. **19**, 153 (2020).

[40] E. Maniv, N. L. Nair, S. C. Haley, S. Doyle, C. John, S. Cabrini, A. Maniv, S. K. Ramakrishna, Y.-L. Tang, P. Ercius, R. Ramesh, Y. Tserkovnyak, A. P. Reyes, and J. G. Analytis, *Antiferromagnetic Switching Driven by the Collective Dynamics of a Coexisting Spin Glass*, Sci. Adv. **7**, eabd8452 (2021).

[41] P. Wadley, B. Howells, J. Železný, C. Andrews, V. Hills, R. P. Campion, V. Novák, K. Olejník, F. Maccherozzi, S. S. Dhesi *et al.*, *Electrical Switching of an Antiferromagnet*, Science **351**, 587 (2016).

[42] S. Y. Bodnar, L. Šmejkal, I. Turek, T. Jungwirth, O. Gomonay, J. Sinova, A. A. Sapozhnik, H. J. Elmers, M. Kläui, and M. Jourdan, *Writing and Reading Antiferromagnetic* Mn_2Au *by Néel Spin-Orbit Torques and Large Anisotropic Magnetoresistance*, Nat. Commun. **9**, 348 (2018).

[43] A. Manchon and S. Zhang, *Theory of Nonequilibrium Intrinsic Spin Torque in a Single Nanomagnet*, Phys. Rev. B **78**, 212405 (2008).

[44] B. V. Laar, H. Rietveld, and D. Ijdo, *Magnetic and Crystallographic Structures of* Me_xNbS_2 *and* Me_xTaS_2, J. Solid State Chem. **3**, 154 (1971).

[45] The identification of any commercial product or trade name does not imply endorsement or recommendation by the National Institute of Standards and Technology, nor does it imply that the materials or equipment identified are necessarily the best available for the purpose.

[46] J. A. Rodriguez, D. M. Adler, P. C. Brand, C. Broholm, J. C. Cook, C. Brocker, R. Hammond, Z. Huang, P. Hundertmark, J. W. Lynn, N. C. Maliszewskyj, J. Moyer, J. Orndorff, D. Pierce, T. D. Pike, G. Scharfstein, S. A. Smee, and R. Vilaseca, *MACS-A New High Intensity Cold Neutron Spectrometer at NIST*, Meas. Sci. Technol. **19**, 034023 (2008).

[47] S. F. Weber and J. B. Neaton, *Origins of Anisotropic Transport in Electrically Switchable Antiferromagnet* $Fe_{1/3}NbS_2$, Phys. Rev. B **103**, 214439 (2021).

[48] V. Dyadkin, F. Mushenok, A. Bosak, D. Menzel, S. Grigoriev, P. Pattison, and D. Chernyshov, *Structural Disorder versus Chiral Magnetism in* $Cr_{1/3}NbS_2$, Phys. Rev. B **91**, 184205 (2015).

[49] N. Doi and Y. Tazuke, *Spin Glass Phases in 2H-*Fe_xNbS_2, J. Phys. Soc. Jpn. **60**, 3980 (1991).

[50] D. C. Johnston, *Influence of Uniaxial Single-Ion Anisotropy on the Magnetic and Thermal Properties of Heisenberg Antiferromagnets within Unified Molecular Field Theory*, Phys. Rev. B **95**, 094421 (2017).

[51] R. J. Birgeneau, H. J. Guggenheim, and G. Shirane, *Spin Waves and Magnetic Ordering in* K_2MnF_4, Phys. Rev. B **8**, 304 (1973).

[52] R. J. Birgeneau, J. Als-Nielsen, and G. Shirane, *Critical Behavior of Pure and Site-Random Two-Dimensional Antiferromagnets*, Phys. Rev. B **16**, 280 (1977).

[53] A. Pelissetto and E. Vicari, *Critical Phenomena and Renormalization-Group Theory*, Phys. Rep. **368**, 549 (2002).

[54] L. Onsager, *Crystal Statistics. I. A Two-Dimensional Model with an Order-Disorder Transition*, Phys. Rev. **65**, 117 (1944).

[55] R. J. Birgeneau, H. Yoshizawa, R. A. Cowley, G. Shirane, and H. Ikeda, *Random-Field Effects in the Diluted Two-Dimensional Ising Antiferromagnet* $Rb_2Co_{0.7}Mg_{0.3}F_4$, Phys. Rev. B **28**, 1438 (1983).

[56] A. S. Wills, *A New Protocol for the Determination of Magnetic Structures Using Simulated Annealing and Representational Analysis (SARAH)*, Physica (Amsterdam) **276-278B**, 680 (2000).

[57] J. Rodriguez-Carvajal, *Fullprof: A Program for Rietveld Refinement and Pattern Matching Analysis*, in *Proceedings*

of the Satellite Meeting on Powder Diffraction of the XV Congress of the IUCr, Toulouse, France, 1990, Vol. 127.

[58] G. L. Squires, *Introduction to the Theory of Thermal Neutron Scattering*, 3rd ed. (Cambridge University Press, Cambridge, England, 2012).

[59] S. Mankovsky, S. Polesya, H. Ebert, and W. Bensch, *Electronic and Magnetic Properties of* $2H-NbS_2$ *Intercalated by* 3*d Transition Metals*, Phys. Rev. B **94**, 184430 (2016).

[60] M. A. Ruderman and C. Kittel, *Indirect Exchange Coupling of Nuclear Magnetic Moments by Conduction Electrons*, Phys. Rev. **96**, 99 (1954).

[61] K. Yosida, *Magnetic Properties of Cu-Mn Alloys*, Phys. Rev. **106**, 893 (1957).

[62] T. Kasuya, *A Theory of Metallic Ferro- and Antiferromagnetism on Zener's Model*, Prog. Theor. Phys. **16**, 45 (1956).

[63] J. B. Goodenough, *Theory of the Role of Covalence in the Perovskite-Type Manganites* $[La, M(II)]Mno_3$, Phys. Rev. **100**, 564 (1955).

[64] J. Kanamori, *Superexchange Interaction and Symmetry Properties of Electron Orbitals*, J. Phys. Chem. Solids **10**, 87 (1959).

[65] D. N. Aristov, *Indirect RKKY Interaction in Any Dimensionality*, Phys. Rev. B **55**, 8064 (1997).

[66] K.-T. Ko, K. Kim, S. B. Kim, H.-D. Kim, J.-Y. Kim, B. I. Min, J.-H. Park, F.-H. Chang, H.-J. Lin, A. Tanaka, and S.-W. Cheong, *RKKY Ferromagnetism with Ising-like Spin States in Intercalated* $Fe_{1/4}TaS_2$, Phys. Rev. Lett. **107**, 247201 (2011).

[67] S. S. P. Parkin, R. Bhadra, and K. P. Roche, *Oscillatory Magnetic Exchange Coupling through Thin Copper Layers*, Phys. Rev. Lett. **66**, 2152 (1991).

[68] S. S. P. Parkin and D. Mauri, *Spin Engineering: Direct Determination of the Ruderman-Kittel-Kasuya-Yosida Far-Field Range Function in Ruthenium*, Phys. Rev. B **44**, 7131 (1991).

[69] S. C. Haley, S. F. Weber, T. Cookmeyer, D. E. Parker, E. Maniv, N. Maksimovic, C. John, S. Doyle, A. Maniv, S. K. Ramakrishna, A. P. Reyes, J. Singleton, J. E. Moore, J. B. Neaton, and J. G. Analytis, *Half-Magnetization Plateau and the Origin of Threefold Symmetry Breaking in an Electrically Switchable Triangular Antiferromagnet*, Phys. Rev. Research **2**, 043020 (2020).

[70] G. H. Wannier, *Antiferromagnetism. The Triangular Ising Net*, Phys. Rev. **79**, 357 (1950).

[71] S. E. Korshunov, *Nature of Phase Transitions in the Striped Phase of a Triangular-Lattice Ising Antiferromagnet*, Phys. Rev. B **72**, 144417 (2005).

[72] A. Smerald, S. Korshunov, and F. Mila, *Topological Aspects of Symmetry Breaking in Triangular-Lattice Ising Antiferromagnets*, Phys. Rev. Lett. **116**, 197201 (2016).

[73] J. Železný, H. Gao, K. Výborný, J. Zemen, J. Mašek, A. Manchon, J. Wunderlich, J. Sinova, and T. Jungwirth, *Relativistic Néel-Order Fields Induced by Electrical Current in Antiferromagnets*, Phys. Rev. Lett. **113**, 157201 (2014).

[74] S. C. Haley, E. Maniv, T. Cookmeyer, S. Torres-Londono, M. Aravinth, J. Moore, and J. G. Analytis, *Long-range, Non-local Switching of Spin Textures in a Frustrated Antiferromagnet*, arXiv:2111.09882.